Multi-Core Fiber Technology for SDM: Coupling Mechanisms and Design

Kunimasa Saitoh , *Member, IEEE, Member, OSA*

(Invited Tutorial)

Abstract—Coupling mechanisms and design issues in multi-core fibers (MCFs) for space division multiplexing are described in this paper. For uncoupled MCFs, a design procedure that considers random structural perturbations and effects of correlation length and birefringence beat length on inter-core crosstalk are presented based on coupled mode theory. Further, for coupled MCFs, a numerical estimation method of modal dispersion is described, and the method to enhance random mode mixing is presented.

Index Terms—Coupled-mode theory, coupled-power theory, few-mode fiber, multi-core fiber, space division multiplexing.

I. INTRODUCTION

TRANSMISSION capacity has been increasing at a rate of 40% per year, which is equivalent to about 100,000 times the capacity in 35 years, since the introduction of the first optical communication system. Various technologies such as time division multiplexing, wavelength division multiplexing, optical amplification, and digital coherent technology have been introduced into commercial systems for increasing the maximum transmission capacity of the single-mode fiber (SMF). With the development of 5G services and the Internet-of-Things (IoT), the current system capacity is expected to increase steadily, and in the 2020s, Peta-b/s class large-capacity systems will be required. However, the maximum transmission capacity of SMF is limited to about 100 Tb/s because of the maximum fiber input power limit, amplifier bandwidth limit, and nonlinear Shannon limit [1]. Space division multiplexing (SDM) is proposed as a next generation technology to extend transmission capacity beyond the limits of conventional SMFs [2]; it is a signal multiplexing technique that utilizes the spatial degree of freedom in an optical fiber.

SDM transmission systems transmit multiple different signals simultaneously by providing multiple spatial paths within an SDM fiber. Fig. 1 illustrates the classification and characteristics of SDM fibers to realize an SDM transmission system. From an optical fiber perspective, there are two approaches for introducing multiple spatial paths into a fiber. The first approach

is utilizing several different modes propagating in a fiber; such a fiber is called a few-mode fiber (FMF). The FMF is a promising scheme in terms of spatial density, which represents the number of spatial channels per unit area, because the number of spatial channels can be scaled up theoretically to more than a few dozen modes within a standard cladding diameter of 125 μm [3]. The second approach for SDM fibers is introducing multiple separate cores in a single fiber; this is known as a multi-core fiber (MCF). The MCFs increase the number of spatial channels by simply increasing the number of cores accommodated in a fiber. In both FMFs and MCFs, multiplexed spatial channels interfere (couple) with each other in the transmission line to some extent. Coupling occurs because of structural perturbations either between modes in FMFs or between adjacent cores in MCFs.

Such SDM fibers can be distinguished by whether each spatial channel is weakly coupled or strongly coupled with other channels. Those that suppress the coupling between different spatial channels as low as possible are classified as uncoupled (or weakly coupled) fibers, and those that allow coupling between spatial channels are classified as coupled (or strongly coupled/randomly coupled) fibers. Weakly coupled FMFs are designed to suppress intra-core mode coupling between different mode groups [4], which results in low complexity multi-input multi-output (MIMO) digital signal processing (DSP) at the receiver to recover the signals. Their refractive index profiles are usually simple step index profiles; however, the upper limit of the channel count is not high. On the other hand, strongly coupled FMFs are designed to reduce differential mode group delay (DMGD) using graded-index profiles. Complex MIMO signal processing is required at the receiver; however, their scalability of the number of channels is high [5]. Similarly, uncoupled MCFs are designed to suppress inter-core mode coupling between adjacent cores [6], which results in no need for MIMO signal processing to compensate for inter-core crosstalk. The channel count can be scaled up by increasing the number of cores while maintaining the sufficiently large core-to-core distance; however, their cladding diameters tend to become larger than 125 μm [7]. In contrast, coupled MCFs are designed to support several different super-modes by intentionally decreasing the core-to-core distance, which results in high spatial density. Coupled MCFs are a type of FMFs, but the most important difference from single-core FMFs is their modal dispersion characteristic. Modal dispersion in single-core FMFs tends to be proportional
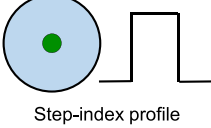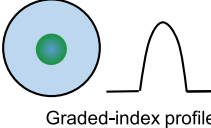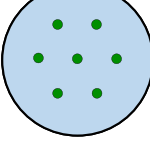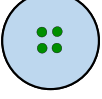
Few-mode fiber (FMF)		Multi-core fiber (MCF)	
Uncoupled (Weakly coupled)	Coupled (Strongly coupled)	Uncoupled (Weakly coupled)	Coupled (Randomly coupled)
Step-index profile	Graded-index profile		
• Limited number of channels • Standard fabrication process • 125 μm diameter clad • Low MIMO complexity	• High number of modes • Standard fabrication process • 125 μm diameter clad • Complex MIMO • Modal dispersion ∝ distance	• High spatial density • Low MIMO complexity • Large cladding diameter	• High spatial density • 125 μm diameter clad • Complex MIMO • Modal dispersion ∝ $\sqrt{\text{distance}}$
Channel count = Number of modes (M)		Channel count = Number of modes (M) x Number of cores (N)	

Fig. 1. Classification and characteristics of SDM fibers.

to the propagation distance, whereas that in coupled MCFs with appropriate core-to-core distance is proportional to the square root of the propagation distance [8].

From the viewpoint of the scalability of the number of spatial channels among the SDM fibers, it becomes difficult to control mode-dependent characteristics in FMFs as increasing the number of modes because of structural fluctuations during fiber fabrication. MCFs can combine mode and core multiplexing. If the number of core multiplexing in the fiber is N and the number of mode multiplexing for each core is M, the number of spatial multiplexing is $N \times M$. Therefore, even if the number of modes M is limited, it is possible to realize an SDM fiber with more than 100 spatial channels using MCFs [9].

In this paper, we focus on MCFs for a long-distance SDM transmission. It is indispensable to understand the basic propagation characteristics to estimate the scalability or potential of MCFs; therefore, we describe coupling mechanisms and design issues in MCFs for SDM. The effect of random perturbations on the inter-core crosstalk in uncoupled MCFs and the modal dispersion in coupled MCFs are discussed based on the coupled mode theory (CMT). For uncoupled MCFs, we review how to consider random structural fluctuations in the transmission line, and we discuss the effect of correlation length and birefringent beat length on inter-core crosstalk. For coupled MCFs, we review how to estimate the modal dispersion numerically and enhance random mode mixing; we discuss the challenging issues in designing coupled MCFs.

II. COUPLING MECHANISMS IN UNCOUPLED MCFS

A. Coupled Mode Theory Without Random Perturbations

Firstly, an MCF with Core m and Core n shown in Fig. 2(a) is considered, wherein the MCF is assumed to have no structural perturbations such as bending and twisting. The coupling characteristics can be described using coupled mode equations given as

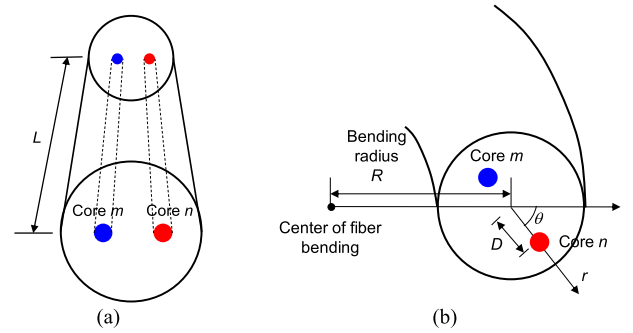$$\frac{da_n(z)}{dz} = -j\beta_n(z)a_n(z) - j\kappa_{nm}(z)a_m(z), \quad (1)$$

Fig. 2. Schematics of MCFs (a) without structural perturbation and (b) with bending and twisting perturbations.

where $a_m(z)$ and $a_n(z)$ represent the mode amplitudes in Core m and Core n, respectively, $\beta_m(z)$ and $\beta_n(z)$ represent the propagation constants in Core m and Core n, $\kappa_{nm}(z)$ denotes the coupling coefficient from Core m to Core n, and z represents the propagation direction. In loss-less MCFs, the coupling coefficients should be symmetric, $\kappa_{nm} = \kappa_{mn}$, to guarantee power conservation [10].

The propagation constants and coupling coefficients are unchanged along the MCF without structural perturbations. When the Core m and Core n are identical ($\beta_m = \beta_n$), which is the case for the homogeneous MCF, the inputted power in Core m changes as shown in Fig. 3(a), where the inputted power in Core m is maximally coupled to Core n after the propagation of the coupling length L_c given by [11]

$$L_c = \frac{\pi}{2\sqrt{\kappa_{nm}^2 + (\Delta\beta_{mn}/2)^2}}, \quad (2)$$

where $\Delta\beta_{mn} = \beta_m - \beta_n$. When each core has different propagation constants ($\beta_m \neq \beta_n$), i.e., a heterogeneous MCF, the maximum power conversion F is greatly suppressed as shown in Fig. 3(b), where F is given by [11]

$$F = \frac{\kappa_{nm}^2}{\kappa_{nm}^2 + (\Delta\beta_{mn}/2)^2}. \quad (3)$$
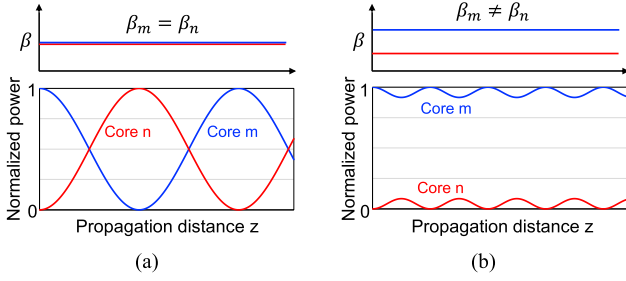
Fig. 3. Mode coupling behavior in the MCF without structural perturbations for (a) homogeneous ($\beta_m = \beta_n$) and (b) heterogeneous ($\beta_m \neq \beta_n$) cores.
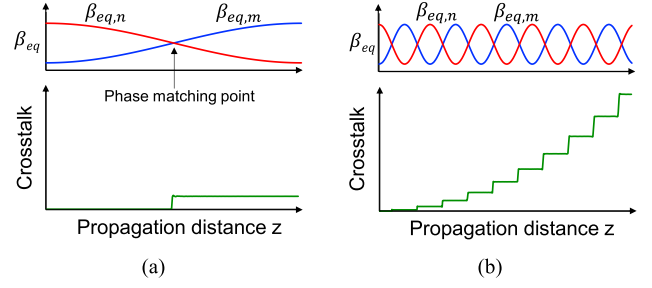

Fig. 4. Relationship between equivalent propagation constant variation along the propagation direction and inter-core crosstalk increase in MCF with bending and twisting perturbations when there are (a) one and (b) ten phase matching points.

In both cases $\beta_m = \beta_n$ and $\beta_m \neq \beta_n$, when MCF has no structural perturbations, the inter-core crosstalk changes periodically, wherein the inter-core crosstalk (XT) is defined by the ratio of the output power $P_n(L)$ in Core n after propagation along an MCF length L and input power $P_m(0)$ in Core m as

$$XT = \frac{P_n(L)}{P_m(0)}. \tag{4}$$

These are well known textbook-based coupling behaviors [11].

An MCF with structural perturbations such as bending and twisting as illustrated in Fig. 2(b) is considered, wherein R denotes the bending radius, θ denotes the twisting angle from the initial horizontal direction, and the distance from the fiber center to the core center of Core m or Core n is assumed to be D. The equivalent propagation constant $\beta_{eq,n}$ in Core n is given by using the bending radius R and twisting angle θ_n as [6]

$$\beta_{eq,n}(z) = \beta_n \left\{ 1 + \frac{D}{R} \cos \theta_n(z) \right\}. \tag{5}$$

Here, we define the equivalent propagation constant difference between Core n and Core m as

$$\Delta \beta_{eq,nm}(z) = \beta_{eq,n}(z) - \beta_{eq,m}(z). \tag{6}$$

Using this $\Delta \beta_{eq,nm}(z)$, the coupled mode equations in MCFs with bending and twisting perturbations can be rewritten as [12]

$$\frac{dA_n(z)}{dz} = -j\kappa_{nm}(z) A_m(z) \exp \{ j\Delta\phi_{nm}(z) \} \tag{7}$$

with

$$a_n(z) = A_n(z) \exp \{ -j\phi_n(z) \}, \tag{8}$$

$$\phi_n(z) = \int_0^z \beta_{eq,n}(z') \, dz', \tag{9}$$

$$\Delta\phi_{nm}(z) = \phi_n(z) - \phi_m(z) = \int_0^z \Delta\beta_{eq,nm}(z') \, dz'. \tag{10}$$

When $\Delta\beta_{eq,mn}(z)$ becomes 0, the phase matching condition between Core m and Core n is satisfied. At this phase matching point, XT increases rapidly similar to the case shown in Fig. 3(a). In other words, we can expect that XT is suppressed except for this phase matching point, and it is similar to the case shown in Fig. 3(b). For example, if there is only one phase matching point along the propagation direction, the XT increase occurs only once as shown in Fig. 4(a). Similarly, the XT increase occurs ten times as shown in Fig. 4(b) if there are ten phase matching points, where this XT evolution occurs only for a specific MCF and is shown for conceptual comparison with Fig. 4(a). These
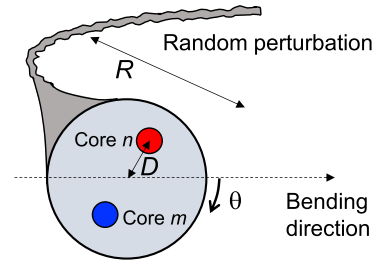

Fig. 5. Schematic of MCF with random structural perturbations.

coupling behaviors are straightforward; however, in a real MCF design, random structural perturbations should be considered.

B. Coupled Mode Theory With Random Perturbations

An MCF with random structural perturbations such as micro-bending and fabrication fluctuations in addition to macro-bending and twisting perturbations is considered, as shown in Fig. 5. Random perturbations in MCFs can be considered by introducing a random phase function into (7), and the coupled mode equations are given as [10]

$$\frac{dA_n(z)}{dz} = -j\kappa_{nm}(z) A_m(z) \exp \{ j\Delta\phi_{nm}(z) \} f_n(z), \tag{11}$$

where $f_n(z)$ denotes the random phase function in Core n. The random phase function is expressed as $f_n(z) = \exp\{j\phi_{rnd}(z)\}$, where $\phi_{rnd}(z)$ denotes the random phase noise at the z position. The random phase noise in each core attributed to random structural perturbation can fluctuate randomly along the propagation direction. Here, it is assumed that the random process of $f_n(z)$ is characterized by an autocorrelation function and correlation length d_s. The autocorrelation function is an unknown function; however, it has been reported that, if the exponential autocorrelation function is assumed, the experimentally measured results of XT in the MCFs fit the analytical ones well [10]. In the following, the random process of $f_n(z)$ is modeled by the exponential autocorrelation function [10] as

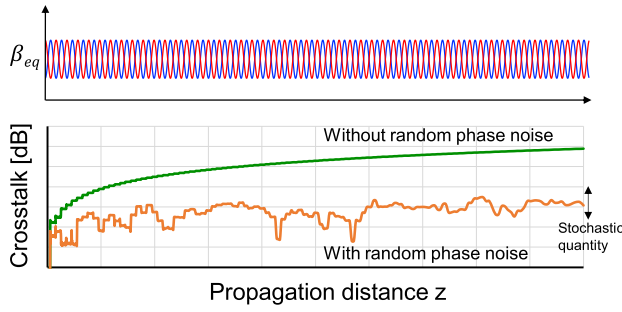$$R_{ff}(z) = \exp \left(-\frac{|z|}{d_s} \right), \tag{12}$$

Fig. 6. Comparison between *XT* without random phase noise and that with random phase noise.

where d_s is the correlation length of random phase function. To obtain the exponential autocorrelation function with the correlation length of d_s, a Wiener process is generated by numerical integration of zero mean white noise with a power spectral density of $2/d_s$. The statistical accuracy of the simulated random process $f_n(z)$ was validated by comparing its autocorrelation function obtained by simulation with the theoretical expression of (12) [10], [13]. The random phase noise $\phi_{rnd}(z)$ is applied independently to all cores, i.e., $f_n(z)$ and $f_m(z)$ are two independent random processes in Core n and m, respectively. The correlation length d_s is a varying parameter for controlling the randomness and it should be sufficiently smaller than the total propagation length L.

Fig. 6 shows a comparison between *XT* without random phase noise and that with random phase noise, where $\Delta\beta_{eq,nm}(z)$ is assumed to become 0 periodically with a constant twisting rate γ along the propagation direction shown in the upper figure in Fig. 6; *XT* evolution is an example for a specific MCF. When there is no random phase noise, *XT* increases constantly with an increase in the propagation distance. On the other hand, when we consider random phase noise, the *XT* changes randomly. The phase offsets between Core n and Core m are different for each phase-matching point, and therefore, the *XT* in Core n increases when the phase offset $f_n(z)$ is in-phase; it decreases when $f_n(z)$ is out-of-phase [6]. Consequently, it is suppressed compared with the case of no random phase noise. The *XT* considering random phase noise is a stochastic quantity, and *XT* evolution is changed at every simulation. Further, when the autocorrelation function of the random process is changed, the stochastic characteristics of the *XT* are changed. However, the averaged value of *XT* in Fig. 6 converges to a constant value when the number of simulations is large; the averaged *XT* can be derived analytically for the autocorrelation function of (12).

When we define the local propagation constant difference at $z = z'$ as $\Delta\beta'_{eq,nm}(z')$, Eq. (11) is approximated near $z = z'$ as [10]

$$\frac{dA_n(z)}{dz} = -j\kappa_{nm}(z) A_m(z) \exp\{j\Delta\beta'_{eq,nm}(z) z\} f_n(z). \tag{13}$$

Although (13) is valid near $z = z'$, we approximate that it can be extended for arbitral z. This is a good approximation except for the case of a long correlation length and very large structural perturbations. The solution of the mode amplitude $A_n(z)$ in (13)

with a random phase function $f_n(z)$ is given by

$$A_n(z) = -j\int_0^z \kappa_{nm}(\zeta) \exp\{j\Delta\beta'_{eq,nm}(z)\zeta\} f_n(\zeta) A_m(0) d\zeta. \tag{14}$$

Then, the averaged crosstalk XT_μ in Core n after the propagation of z can be expressed as [10], [14]

$$XT_\mu(z) = z \times \kappa_{nm}^2 \int_{-\infty}^{+\infty} \exp\{j\Delta\beta'_{eq,nm}(z)\zeta\} R_{ff}(\zeta) d\zeta, \tag{15}$$

where $R_{ff}(\zeta)$ is the autocorrelation function of the random process of $f_n(\zeta)$. As mentioned earlier, the exponential autocorrelation function is adequate for fitting experimentally measured results to numerical ones [10]. By using the exponential autocorrelation function expressed as (12), the averaged crosstalk XT_μ after the propagation of z can be obtained using the Lorentzian function as

$$XT_\mu(z) = z \times \frac{2\kappa_{nm}^2 d_s}{1+\Delta\beta'^2_{eq,nm}(z)d_s^2} = z \times h(z), \tag{16}$$

where the Lorentzian function, $h(z)$, denotes the power coupling coefficient at the z position, which is the amount of *XT* per unit length. The averaged XT_μ given by (16) is based on the coupled power theory (CPT) [10], [14].

Fig. 7 shows the mean XT_μ as a function of R in two core MCFs with several different values of d_s, where we assume that the MCF is bent at a constant radius and twisted continuously at a constant twisting rate $\gamma = 0.1\pi$ rad/m; the wavelength is 1550 nm. Green, blue, and red results represent the averaged XT_μ for correlation lengths of 10 m, 1 m, and 0.1 m, respectively. The solid curves are results evaluated from the averaged power coupling coefficient h based on (16), where $h(z)$ is averaged over a twisting period. For comparison, the solid circle plots are presented, and they are obtained by directly solving the coupled mode equations of (11), where XT_μ is calculated from the average of 100 calculation results. Fig. 7(a) shows the results for an ideal homogeneous MCF ($\beta_m = \beta_n$) with $a = 4.5$ μm, $\Delta = 0.35\%$, and $\Lambda = 45$ μm. The refractive index of the cladding is $n_{clad} = 1.45$. When the bending radius is smaller than 10 m, the averaged XT_μ almost does not depend on the correlation length and linearly increases with an increase in R. This relation is well approximated as [6]

$$h = \frac{2\kappa_{nm}^2 R}{\beta_n \Lambda}. \tag{17}$$

When R is very large like in an almost straight fiber, the averaged XT_μ decreases with a decrease in the correlation length. Thus, *XT* can be reduced by simply shortening d_s in the MCFs with a very large R. However, this is not the case in real scenarios. Because in an actual MCF, there will be different fabrication errors for each core even if it is fabricated as a homogeneous MCF. Fig. 7(b) shows the results for heterogeneous MCFs ($\beta_m \neq \beta_n$) with a small fabrication error in each core, where $a = 4.5$ μm, $\Lambda = 45$ μm, and it is assumed that each core has a core $\Delta = 0.35 \pm 0.001\%$. The refractive index of the cladding is $n_{clad} = 1.45$. Contrary to the homogeneous MCFs, XT_μ decreases with an increase in the correlation length in heterogeneous MCFs when R is larger than the critical bending
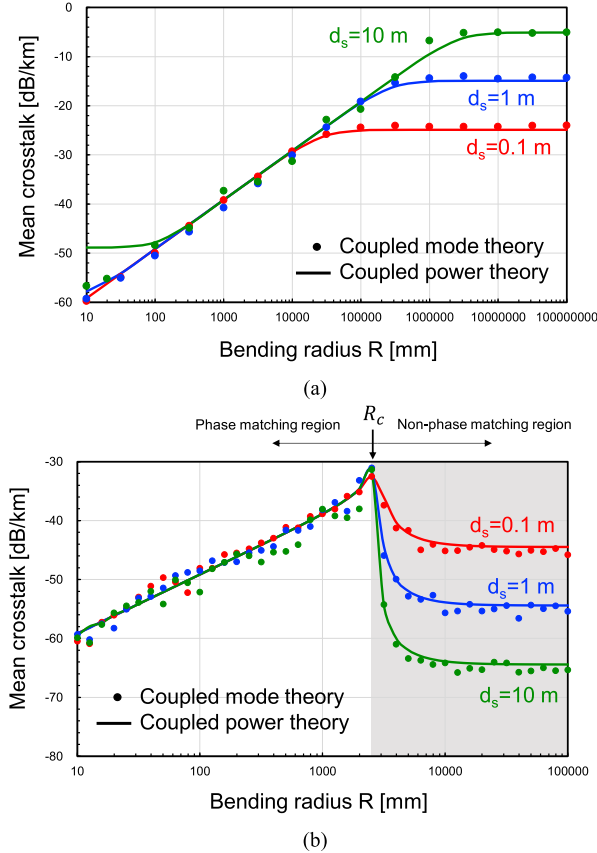
(a)

(b)

Fig. 7. Mean XT_μ in MCFs with $a = 4.5$ μm and $\Lambda = 45$ μm as a function of bending radius R evaluated from the averaged power coupling coefficient h (solid curves) and the coupled mode equations (circle plots) for (a) homogeneous MCFs ($\beta_m = \beta_n$) with $\Delta = 0.35\%$ and (b) heterogeneous MCFs ($\beta_m \neq \beta_n$) with $\Delta = 0.35 \pm 0.001\%$, where the twisting rate is assumed to be $\gamma = 0.1\pi$ rad/m and $n_{clad} = 1.45$.

radius, R_c, where R_c is given by using the averaged propagation constant of $\beta_{ave} = (\beta_n + \beta_m)/2$ and intrinsic propagation constant difference between cores of $|\beta_n - \beta_m|$ as [6]

$$R_c = \frac{\beta_{ave}\Lambda}{|\beta_n - \beta_m|} . \tag{18}$$

If the bending perturbation is dominant, i.e., $R < R_c$, XT is determined by phase matching between cores, and therefore, the averaged XT_μ is weakly dependent on the correlation length. On the contrary, when the bending perturbation is weak, i.e., $R > R_c$, there is no phase matching point along the propagation direction, and XT strongly depends on the correlation length. Therefore, in heterogeneous MCFs with non-phase matching region, the correlation length should be increased, i.e., "randomness" should be decreased to as good as possible for decreasing XT.

These results indicate that both CMT results (circle plots) obtained via (11) and the CPT results (solid curves) obtained using (16) are in good agreement in most cases when we consider the same autocorrelation function of random processes, as shown in Fig. 7. Further, Eq. (16) yields a reasonably correct estimation of the averaged XT_μ. However, Eq. (13) is an approximated expression of (11), and it has been recently reported that the averaged XT_μ obtained by (16) may result in a difference of more than 6 dB compared to the rigorous estimation based on
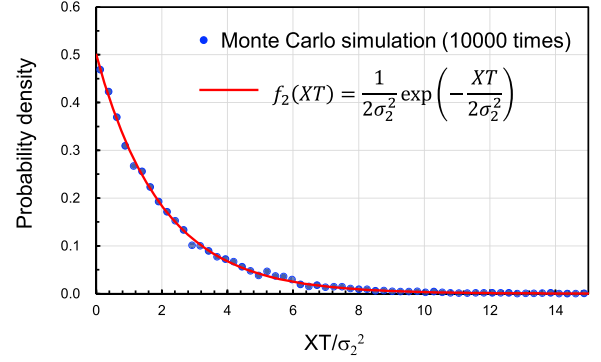

Fig. 8. Probability density distribution calculated by using (11) for an MCF with $a = 4.5$ μm, $\Delta = 0.35\%$, $\Lambda = 45$ μm, $n_{clad} = 1.45$, $d_s = 1$ m, $\gamma = 0.1\pi$ rad/m, and $R = 140$ mm at $\lambda = 1550$ nm. The solid circle plots indicate results obtained using Monte Carlo simulations with (11) over 10,000 repetitions, where the horizontal axis is normalized by the variance σ_2^2.

(11), especially in the case of a large twisting rate and large correlation length [13]. In Fig. 7(a), the difference between CMT and CPT becomes larger than 5 dB for very small R ($R < 50$ mm) with a large d_s of 10 m. This difference is originating from the approximated (13) in CPT. In [13], a more rigorous analytical expression was reported for evaluating the power coupling coefficient and the averaged XT_μ in uncoupled MCFs.

Thus far, it was shown that the power coupling coefficient $h(z)$ in (16) can be used to estimate the reasonably accurate mean XT_μ in uncoupled MCFs in most practical cases; however, XT is a stochastic quantity and changes to some extent by time variation or wavelength change. The probability density distribution of XT can be easily obtained by repeating numerical simulation. Fig. 8 shows the numerically obtained probability density distribution of the inter-core XT for an MCF with $a = 4.5$ μm, $\Delta = 0.35\%$, $\Lambda = 45$ μm, and $n_{clad} = 1.45$. Further, $R = 140$ mm, $\lambda = 1550$ nm, $d_s = 1$ m, and $\gamma = 0.1\pi$ rad/m. The solid circle plots indicate results obtained using Monte Carlo simulations with (11) over 10,000 repetitions, where the horizontal axis is normalized by the variance σ_2^2. We see that it looks like Chi-square distribution with 2 degrees of freedom. The solid line in Fig. 8 shows the fitting curve of the Chi-square distribution with 2 degrees of freedom, $f_2(XT)$, which is expressed as [15]

$$f_2(XT) = \frac{1}{2\sigma_2^2} \exp\left(-\frac{XT}{2\sigma_2^2}\right). \tag{19}$$

The dotted results obtained by CMT are well fitted by the solid curve. This Chi-square distribution with 2 degrees of freedom is attributed to the fact that the complex field $A_n(z)$ in (11) has two components: its in-phase (real) and quadrature (imaginary) components. Based on the central limit theorem, the probability density function of each component converges to a normal distribution. Therefore, the total probability density distribution results in a Chi-square distribution with 2 degrees of freedom, where the variance σ_2^2 in the phase matching region is expressed using the propagation distance L as [15]

$$\sigma_2^2 = \frac{\kappa_{nm}^2}{\beta_n} \frac{R}{\Lambda} L. \tag{20}$$

In the actual fibers, the field in each core has two polarization components and they are randomly coupled with each other. When we assume that optical power is distributed to two polarization modes in equal probabilities, the power is distributed to in-phase and quadrature components of the two polarization modes [15]. Therefore, the probability density distribution of *XT* in actual MCFs becomes a Chi-square distribution with 4 degrees of freedom [15]–[18] and (11) is insufficient to fully simulate the mode coupling phenomenon in MCFs.

C. Coupled Mode Theory With Polarization Mode Coupling

In the coupled mode equations shown in (11), we consider the scalar field in each core, i.e., only the scalar coupling between each core is considered. However, in a real scenario, polarization mode coupling also exists in each core. A new term for polarization mode coupling can be introduced into the coupled mode equations to consider polarization mode coupling for MCF design as [19]

$$
\begin{aligned}
&\frac{d\boldsymbol{A}_n(z)}{dz} \\
&= -j\kappa_{nm}(z)\exp\{j\Delta\phi_{nm}(z)\}\begin{bmatrix} f_{xn}(z) & 0 \\ 0 & f_{yn}(z) \end{bmatrix}\boldsymbol{A}_m(z) \\
&\quad -j\frac{\boldsymbol{b}_n(z)\cdot\boldsymbol{\sigma}}{2}\boldsymbol{A}_n(z)
\end{aligned}
\tag{21}
$$

with

$$
\boldsymbol{A}_n(z) = \begin{bmatrix} A_{xn}(z) & A_{yn}(z) \end{bmatrix}^T, \tag{22}
$$

where the second term on the right side in (21) represents polarization mode coupling, field amplitude in Core n becomes vector $\boldsymbol{A}_n(z)$, and ^{T} represents the transpose. $A_{xn}(z)$ and $A_{yn}(z)$ are the horizontal (x) and vertical (y) components of the field amplitude, respectively. $f_{xn}(z)$ and $f_{yn}(z)$ represent the x and y components of the random phase function in Core n, where it is assumed that each component has independent random processes with the same autocorrelation function shown in (12). $\boldsymbol{b}_n(z)$ denotes the birefringence vector in Core n, and $\boldsymbol{\sigma}$ represents the well-known three Pauli matrices given by

$$
\sigma_x = \begin{bmatrix} 1 & 0 \\ 0 & -1 \end{bmatrix}, \quad \sigma_y = \begin{bmatrix} 0 & 1 \\ 1 & 0 \end{bmatrix}, \quad \sigma_z = \begin{bmatrix} 0 & -j \\ j & 0 \end{bmatrix}. \tag{23}
$$

$\boldsymbol{b}_n(z)$ has three components of $b_{xn}(z)$, $b_{yn}(z)$, and $b_{zn}(z)$; however, in telecommunication fibers, the third component, which describes circular birefringence, is negligible. Therefore, it is assumed that the third component of the birefringence vector is zero, i.e., $b_{zn}(z) = 0$ [19]. This model is known as the random modulus model (RMM) [20]. The first and second components of the birefringence vector are modeled by independent Ornstein-Uhlenbeck random processes with a correlation function $R_{b_n}(z)$ given by [19], [20]

$$
R_{b_n}(z) = \frac{1}{2}\left(\frac{2\pi}{L_B}\right)^2\exp\left(-\frac{|z|}{d_p}\right), \tag{24}
$$

where L_B denotes the beat length of the fiber birefringence and d_p denotes the correlation length of the birefringence vector. The correlation length d_s of the random phase noise and the correlation length d_p of the random birefringence vector are independent parameters.
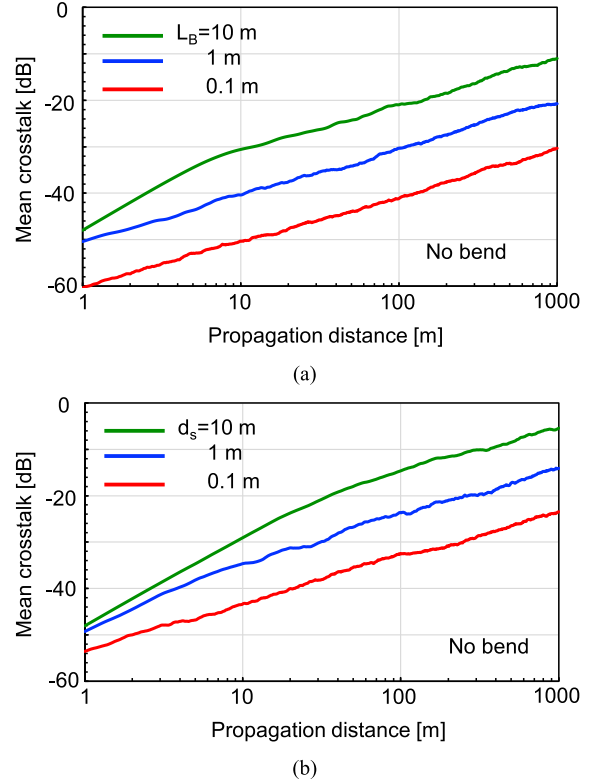

(a)

(b)

Fig. 9.   Mean *XT* as a function of propagation distance for an MCF calculated by using (21) (a) without considering random phase noise and (b) without considering polarization mode coupling, where $a = 4.5\,\mu$m, $\Delta = 0.35\%$, $\Lambda = 45\,\mu$m, $n_{clad} = 1.45$, $\lambda = 1550$ nm, the fiber is assumed to have no bending perturbation, and *XT* is obtained from the average of 100 calculation results.

The averaged crosstalk XT_μ in Core n after propagation of z considering polarization mode coupling can be approximated by

$$
\begin{aligned}
XT_\mu(z) &= z\kappa_{nm}^2 \\
&\times \int_{-\infty}^{+\infty}\exp\{j\Delta\beta'_{eq,nm}(z)\zeta\}R_n(\zeta)R_{ff}(\zeta)R_m(\zeta)\,d\zeta,
\end{aligned}
\tag{25}
$$

where $R_n(\zeta)$ and $R_m(\zeta)$ are autocorrelation functions describing the polarization mode coupling effect in Core n and m, respectively [19].

In the following, we numerically evaluate the mode coupling characteristics in uncoupled MCFs using CMT with a polarization mode coupling term given as (21), and it is assumed that the birefringence vector is characterized by the same statistics in all cores, i.e., $R_{b_n}(z) = R_{b_m}(z)$. The components of the birefringence vector from different cores are independent processes and the exponential autocorrelation function shown in (24) is used.

Fig. 9 shows the mean *XT* as a function of the propagation distance for an MCF, where $a = 4.5\,\mu$m, $\Delta = 0.35\%$, $\Lambda = 45\,\mu$m, $n_{clad} = 1.45$, $\lambda = 1550$ nm, and the fiber does not have bending perturbation, i.e., the fiber is assumed to be straight. *XT* was calculated from the average of 100 calculation results. Fig. 9(a) shows the results for several different values of the birefringence beat length L_B calculated using (21) without considering the random phase noise, wherein d_p is assumed to be equal to L_B as an example. We see that *XT* decreases with a decrease in
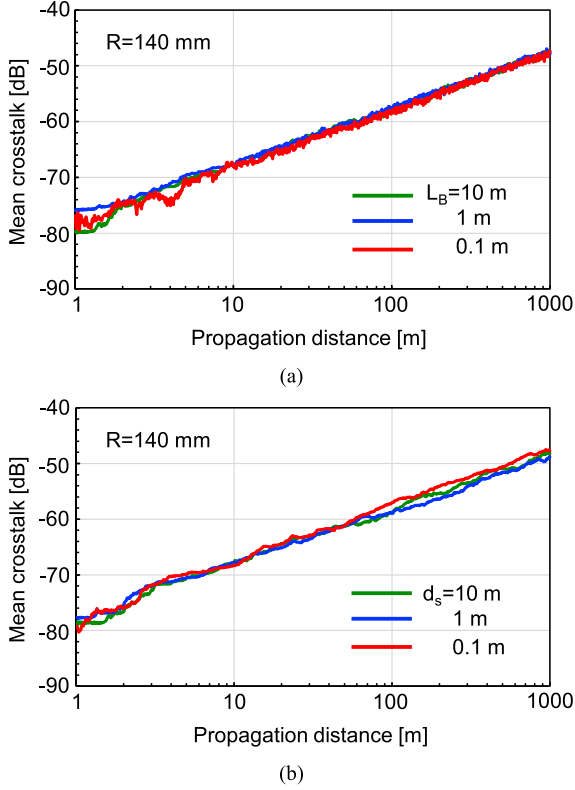
(a)

(b)

Fig. 10. Mean *XT* as a function of propagation distance for an MCF calculated by using (21) (a) without considering random phase noise and (b) without considering polarization mode coupling, where $a = 4.5$ μm, $\Delta = 0.35\%$, $\Lambda = 45$ μm, $n_{clad} = 1.45$, $\lambda = 1550$ nm, $\gamma = 0.1\pi$ rad/m, the fiber is assumed to be bent with $R = 140$ mm, and *XT* is obtained from the average of 100 calculation results.

L_B. For comparison, Fig. 9(b) shows the results for several different values of d_s, calculated using (21) without considering the polarization mode coupling term. Similar results as shown in Fig. 9(a) are obtained by changing d_s, even if we do not consider polarization mode coupling.

Similarly, Fig. 10 shows the mean *XT* as a function of propagation distance for an MCF, where $a = 4.5$ μm, $\Delta = 0.35\%$, $\Lambda = 45$ μm, $n_{clad} = 1.45$, $\lambda = 1550$ nm, and the fiber is assumed to be bent with $R = 140$ mm and $\gamma = 0.1\pi$ rad/m. The *XT* was calculated from the average of 100 calculation results. Fig. 10(a) shows the results for several different values of L_B calculated using (21) without considering random phase noise, where d_p is assumed to be equal to L_B, which is the same as that in Fig. 9(a). Fig. 10(b) shows the results for several different values of d_s calculated using (21) without considering the polarization mode coupling term. We confirm that both approaches shown in Figs. 10(a) and (b) yield similar *XT* behaviors. In Fig. 10(a), constant (intrinsic) bending and twisting perturbations as well as random polarization coupling perturbation are considered in the phase matching region. In this case, the *XT* change occurs almost discretely at the phase matching point even if the long birefringent beat length and long correlation length of the random polarization coupling perturbation are considered. Therefore, the *XT* curves in Fig. 10(a) are similar to those in Fig. 10(b). However, the probability density distribution of *XT*
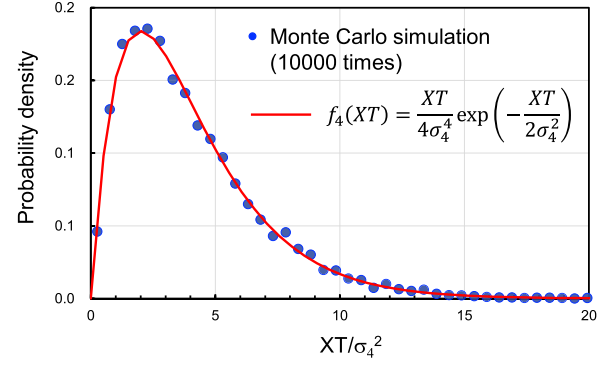
in Fig. 10(a) may be different from that in Fig. 10(b). Because, in Fig. 10(b), when *x*-component $(A_{xm}(0))$ or *y*-component $(A_{ym}(0))$ is inputted at $z = 0$, the power is distributed to only *x*- or *y*-component, respectively.

Fig. 11 shows numerically obtained probability density distribution of *XT* with the polarization mode coupling for an MCF, where $a = 4.5$ μm, $\Delta = 0.35\%$, $\Lambda = 45$ μm, and $n_{clad} = 1.45$. Here, $R = 140$ mm, $\lambda = 1550$ nm, $\gamma = 0.1\pi$ rad/m, and $L_B = d_p = 1$ m. The solid circle plots represent results obtained via Monte Carlo simulations using (21) with 10,000 repetitions, where the horizontal axis is normalized by the variance σ_4^2. It appears like Chi-square distribution with 4 degrees of freedom. The solid line in Fig. 11 shows the fitting curve of the Chi-square distribution with 4 degrees of freedom, $f_4(XT)$, which is expressed as

$$f_4(XT) = \frac{XT}{4\sigma_4^4} \exp\left(-\frac{XT}{2\sigma_4^2}\right), \quad (26)$$

where the variance σ_4^2 in the phase matching region is expressed using the propagation distance L as [15]

$$\sigma_4^2 = \frac{1}{2} \frac{\kappa_{nm}^2}{\beta_n} \frac{R}{\Lambda} L. \quad (27)$$

The dotted results obtained by the CMT with the polarization mode coupling are well fitted by the solid curve; they are consistent with the measured probability density distribution of *XT* in actual MCFs [15].

Next, the bending radius dependence of the mean *XT* in MCFs with the polarization mode coupling effect is considered. Fig. 12 shows the mean *XT* as a function of R with several different values of L_B calculated using (21), where the fiber is an ideal homogeneous MCF with $a = 4.5$ μm, $\Delta = 0.35\%$, and $\Lambda = 45$ μm, and $\gamma = 0.1\pi$ rad/m. The mean *XT* is calculated from the average of 100 calculation results at $\lambda = 1550$ nm and d_p is assumed to be equal to L_B. Green, blue, and red results represent the mean *XT* for beat length of 10 m, 1 m, and 0.1 m, respectively. When the bending radius is smaller than 10 m, the mean *XT* does not depend on the beat length L_B, and it linearly increases with an increase in R. In this bending perturbation dominant

Fig. 11. Probability density distribution calculated using (21) for an MCF with $a = 4.5$ μm, $\Delta = 0.35\%$, $\Lambda = 45$ μm, $n_{clad} = 1.45$, $L_B = d_p = 1$ m, $\gamma = 0.1\pi$ rad/m, and $R = 140$ mm at $\lambda = 1550$ nm. Solid circle plots represent results obtained via Monte Carlo simulations with 10,000 repetitions and the solid line represents the fitting curve of the Chi-square distribution with 4 degrees of freedom, where the horizontal axis is normalized by the variance σ_4^2.
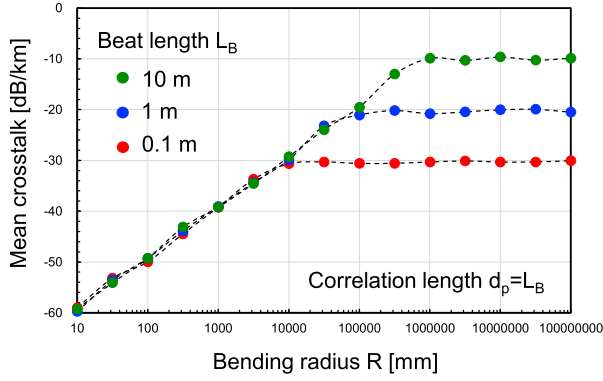
Fig. 12. Mean *XT* as a function of *R* with the fiber beat length $L_B = 10$ m, 1 m, and 0.1 m, where the fiber is an ideal homogeneous MCF with $a = 4.5$ μm, $\Delta = 0.35\%$, $\Lambda = 45$ μm, and $n_{clad} = 1.45$, and it is assumed to have the constant twisting rate of 0.1π rad/m.
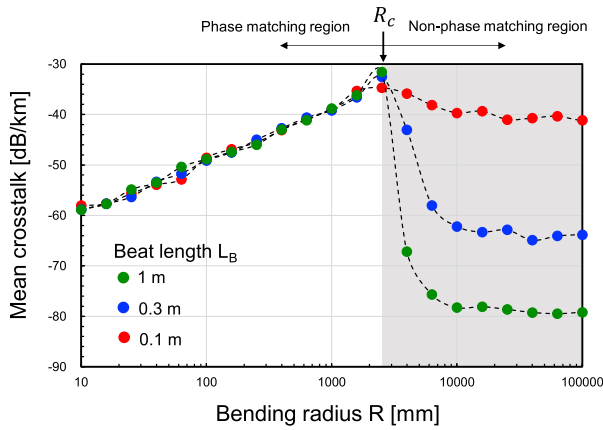

Fig. 13. Mean *XT* in a two core MCF with small fabrication error as a function of bending radius *R* with the fiber beat length $L_B = 1$ m, 0.3 m, and 0.1 m, where $a = 4.5$ μm, $\Lambda = 45$ μm, $n_{clad} = 1.45$, the constant twisting rate $\gamma = 0.1\pi$ rad/m, and it is assumed that each core has the core $\Delta = 0.35 \pm 0.001\%$.

region, the mean *XT* does not depend on whether $L_B = d_p$ or $L_B \neq d_p$. On the other hand, when the bending radius is very large like in an almost straight fiber, the mean *XT* decreases with a decrease in the beat length L_B. In this weak bending perturbation region, the mean *XT* not depend on d_p when $d_p \geq L_B$, whereas it increases as decreasing d_p when $d_p < L_B$ [19]. Thus, *XT* can be decreased by decreasing L_B in MCFs with very large *R*. However, this is not the case in a real scenario. In an actual MCF, even if it is fabricated as a homogeneous MCF, each core has different fabrication errors. In this case, the result shown in Fig. 12 is changed.

Fig. 13 shows the mean *XT* in a two core MCF with a small fabrication error as a function of *R* with several different values of L_B calculated using (21), where $a = 4.5$ μm, $\Lambda = 45$ μm, $n_{clad} = 1.45$, $\gamma = 0.1\pi$ rad/m, and it is assumed that each core has the core $\Delta = 0.35 \pm 0.001\%$. The mean *XT* is calculated from the average of 100 calculation results at $\lambda = 1550$ nm and d_p is assumed to be equal to L_B. Green, blue, and red results represent the mean *XT* for L_B of 1 m, 0.3 m, and 0.1 m, respectively. When $R > R_c$, the mean *XT* increases with a decrease in the beat length. Therefore, in the non-phase matching
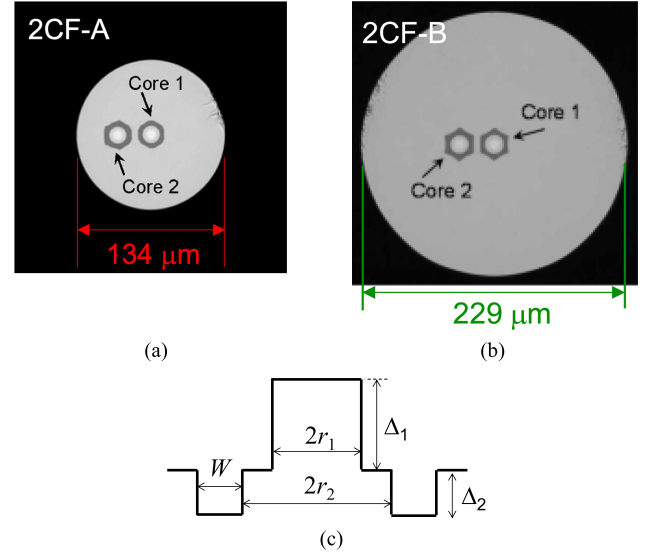

(a)

(b)

(c)

Fig. 14. Cross-sectional view of fabricated heterogeneous two-core MCFs of (a) 2CF-A and (b) 2CF-B, which were reported in [21]. Both fibers have almost the same core parameters with (c) a step-index profile with low-index trench; however, the cladding diameter in 2CF-A is 134 μm and that in 2CF-B is 229 μm.

TABLE I
CORE PARAMETERS FOR CORE 1 AND CORE 2 [22]

	r_1 [μm]	r_2/r_1	W/r_1	Δ_1 [%]	Δ_2 [%]
Core 1	4.62	1.7	1.0	0.305	−0.7
Core 2	4.47	1.7	1.2	0.273	−0.7

region, "randomness" should be decreased to as good as possible for decreasing *XT*.

Thus, it is possible to compare the experimentally measured *XT* and numerically evaluated one by considering d_p and L_B as fitting parameters; therefore, the correlation length and beat length in the fabricated MCFs can be estimated. Fig. 14 shows the cross-al view of the fabricated heterogeneous two-core MCFs (2CF-A and 2CF-B), reported in [21]. Both MCFs have almost the same core parameters of the effective mode area $A_{eff} \approx 78$ μm^2; however, the cladding diameter of 2CF-A (Fig. 14(a)) is 134 μm and that of 2CF-B (Fig. 14(b)) is 229 μm. Each core has a step-index profile with a low index trench as shown in Fig. 14(c). The fiber parameters of Core 1 and Core 2 are listed in Table I [22]. The core-to-core distance Λ is 29.9 μm and 29.7 μm in 2CF-A and 2CF-B, respectively [21]. The MCF with a larger cladding diameter will have lower random fluctuations because of perturbations such as micro-bending, which results in lower *XT*. In [21], the *XT* was measured by changing the winding tension with $R = 155$ mm. When the winding tension is varied from 0 to 250 gf, the range of the measured *XT* was −68 dB/km to −52 dB/km in 2CF-A with a cladding diameter of 134 μm, while it was −74 dB/km to −65 dB/km in 2CF-B with cladding diameter of 229 μm. The increase in the winding tension results in an increase in the randomness, which consequently increases the inter-core *XT* in the non-phase matching region. Fig. 15 shows the numerically evaluated mean
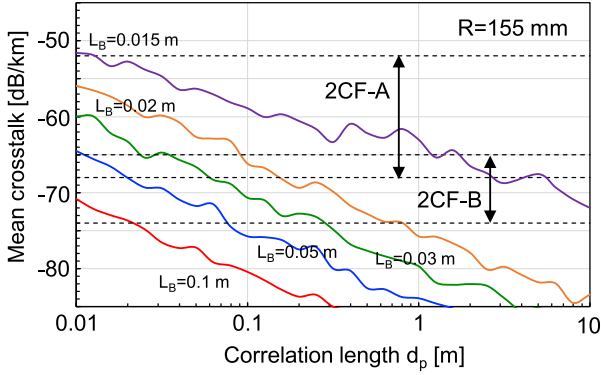
Fig. 15. Numerically evaluated mean *XT* in 2CF-A and 2CF-B shown in Fig. 15 [21] by varying d_p and L_B, where $R = 155$ mm, the constant twisting rate is assumed to be $\gamma = 0.1\pi$ rad/m, and the mean *XT* is calculated from the average of 100 calculation results at $\lambda = 1550$ nm.

Fig. 16. (a) Design parameters of MCFs and (b) graded index profile with low index trench.

TABLE II
PARAMETERS FOR 2LP-, 4LP-, 6LP-, AND 9LP-MODE CORES

	2LP	4LP	6LP	9LP
r_1 [μm]	8.3	9.6	10.8	11.8
r_2 [μm]	10.0	11.0	12.1	13.0
W/r_1	0.77	0.67	0.58	0.51
Δ_1 [%]	0.62	0.82	1.00	1.20
Δ_2 [%]	−0.7	−0.7	−0.7	−0.7

Fig. 17. Bending loss in 2LP-, 4LP-, 6LP-, and 9LP-mode cores as a function of CT at $\lambda = 1565$ nm, where $R = 140$ mm.

XT in 2CF-A and 2CF-B by varying d_p and L_B, where $R = 155$ mm, the twisting rate is assumed to be $\gamma = 0.1\pi$ rad/m, and the mean *XT* is calculated from the average of 1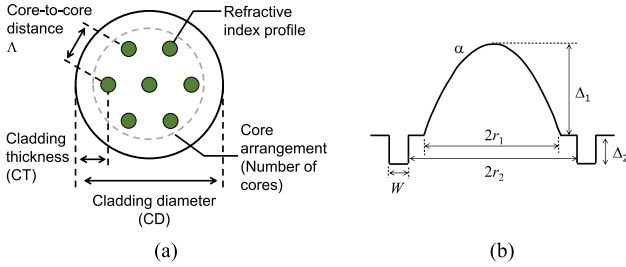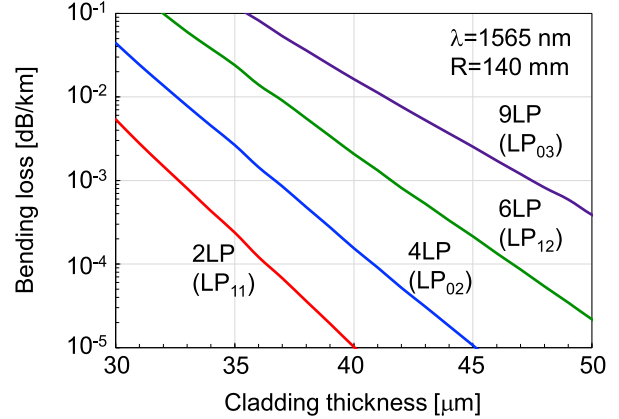00 calculation results at $\lambda = 1550$ nm. $R = 155$ mm corresponds to the value experimentally used in [21]. The two arrows in Fig. 15 represent the range of experimentally measured *XT* in [21]. As expected, a smaller beat length and/or correlation length increases randomness, which results in an increase in the inter-core *XT*. L_B can be estimated to be around 50 mm by comparing the range of the measured *XT* [21]; further, d_p seems to be on the order of L_B. From this result, the polarization mode dispersion (PMD) coefficient in the fabricated MCF [21] is estimated to be in the order of sub ps/$\sqrt{km}$, which is consistent with the recently reported findings [23]. This is not a general conclusion, but a fabricated MCF tends to have a shorter birefringence beat length, namely larger PMD, compared with that of SMFs, because of the difference in the fabrication process.

III. SCALABILITY AND DESIGN ISSUES IN UNCOUPLED MCFS

Fig. 16(a) shows the design parameters of MCFs. The refractive index profile is determined based on the A_{eff}, DMGD, and cutoff wavelength in each core. The core-to-core distance Λ is determined based on the allowable *XT* level between cores. The clad thickness (CT), which is the distance from the clad edge to the core center of the outermost core, is designed such that the confinement loss is at a sufficiently low level of about 10^{-3} dB/km [24]. The number of cores and the core arrangement

are related to spatial density, and the upper clad diameter (CD) is determined based on mechanical reliability [25] and fiber productivity.

We estimate the scalability of the spatial density in uncoupled MCFs with the combination of core multiplexing and mode multiplexing considering these design requirements. When designing uncoupled MCFs wherein multiple modes propagate in each core, a graded index profile with low index trench shown in Fig. 16(b) is widely used for index profile in each core [26]–[30]. If the inter-core *XT* is sufficiently small, each core can be used for coupled FMF independently. The graded index core is suitable for reducing DMGD in each core and the low index trench is effective in reducing inter-core *XT* and bending loss. Table II summarizes typical structural parameters for 2LP-mode (3-mode), 4LP-mode (6-mode), 6LP-mode (10-mode), and 9LP-mode (15-mode) cores [26]–[30], where the graded index shape factor α is assumed to be 2.0. Each core profile is designed to have the A_{eff} of approximately 80 μm^2 for the fundamental mode (LP$_{01}$ mode) at a wavelength of 1550 nm and the maximum DMGD of less than a few hundred ps/km in the entire C-band. The trench width W is determined to maintain the cutoff wavelength below 1530 nm, where the relative trench width W/r_1 must be reduced as the number of modes is increased.

The required CT can be estimated by evaluating the bending loss of the outermost core. Fig. 17 shows calculated bending losses for LP$_{11}$, LP$_{02}$, LP$_{21}$, and LP$_{03}$ modes as a function of CT at a wavelength of 1565 nm in the 2LP-, 4LP-, 6LP-, and 9LP-mode cores, respectively, wherein the core parameters listed in Table II were used; $R = 140$ mm, and the vector finite element method (FEM) [31] was used for calculations. The CT must be
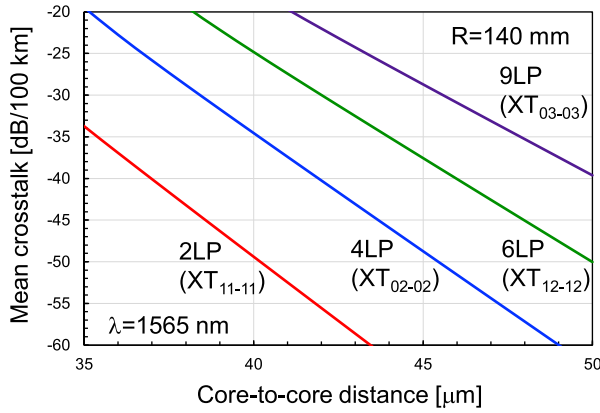
Fig. 18. Mean XT between LP$_{11}$ (XT$_{11\text{-}11}$), LP$_{02}$ (XT$_{02\text{-}02}$), LP$_{12}$ (XT$_{12\text{-}12}$), and LP$_{03}$ modes (XT$_{03\text{-}03}$), in the 2LP-, 4LP-, 6LP-, and 9LP-mode cores, respectively, as a function of core-to-core distance at $\lambda = 1565$ nm.

TABLE III
CT AND Λ FOR 2LP-, 4LP-, 6LP-, AND 9LP-MODE MCFs

	2LP	4LP	6LP	9LP
CT [μm]	32.7	36.7	41.6	47.5
Λ [μm]	35.4	40.2	44.0	47.9

increased with an increase in the number of modes, and to keep the bending loss below 10^{-3} dB/km at $\lambda = 1565$ nm; at least CTs of 32.7 μm, 36.7 μm, 41.6 μm, and 47.5 μm are required for 2LP-, 4LP-, 6LP-, and 9LP-mode operation, respectively. If the bending loss is lower than 10^{-3} dB/km, the contribution to the total transmission loss can be considered to be at a sufficiently small level.

The required core-to-core distance Λ can be estimated by evaluating the mean XT between neighboring cores. Fig. 18 shows the mean XT between LP$_{11}$ (XT$_{11\text{-}11}$), LP$_{02}$ (XT$_{02\text{-}02}$), LP$_{12}$ (XT$_{12\text{-}12}$), and LP$_{03}$ modes (XT$_{03\text{-}03}$) as a function of Λ at a wavelength of 1565 nm in the 2LP-, 4LP-, 6LP-, and 9LP-mode cores, respectively, calculated by using (16), where core parameters summarized in Table II are used, $R = 140$ mm, and $d_s = 50$ mm. XT$_{11\text{-}11}$, XT$_{02\text{-}02}$, XT$_{12\text{-}12}$, and XT$_{03\text{-}03}$ provide the worst-case XT in 2LP-, 4LP-, 6LP-, and 9LP-mode MCFs, respectively, because the higher-order mode has a relatively large A_{eff} compared to that of the LP$_{01}$ mode, and the confinement of higher-order modes is weaker than that of the LP$_{01}$ mode [32]. Λ needs to be increased as the number of modes increases to achieve a similar XT level. For example, if the allowable XT between two cores is -35 dB/100 km, the required Λ for 2LP-, 4LP-, 6LP-, and 9LP-mode operation are at least 35.4 μm, 40.2 μm, 44.0 μm, and 47.9 μm, respectively. The mean XT of -35 dB/100 km between two cores corresponds to the worst-case crosstalk XT_{worst} of -27 dB/100 km when considering six adjacent cores; it is for realizing the 1000 km transmission of QPSK signals with a power penalty of less than 1 dB [33].

Table III summarizes the designed parameters of CT and Λ for uncoupled MCFs with 3–15 propagation modes in each core. Based on these design parameters, the scalability of relative spatial density in uncoupled MCFs as a function of CD is shown in Fig. 19, wherein the relative spatial density is defined by
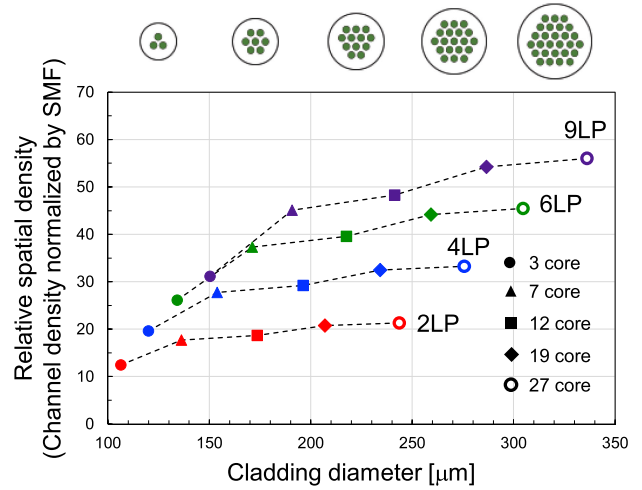

Fig. 19. Scalability of relative spatial density in uncoupled MCFs as a function of CD, where hexagonally arranged 3, 7, 12, 19, and 27 cores are assumed.
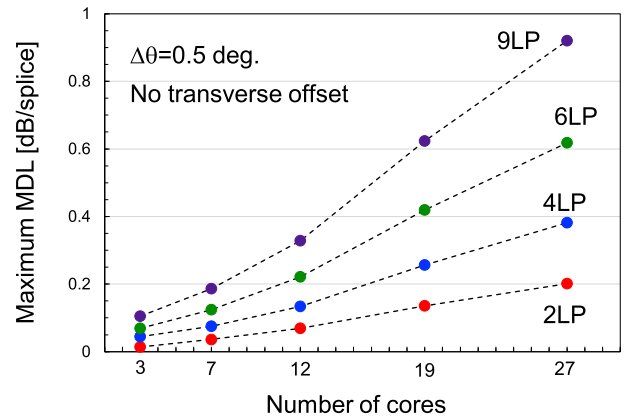

Fig. 20. Maximum MDL at splicing point at $\lambda = 1550$ nm as a function of number of cores for 2LP-, 4LP-, 6LP-, and 9LP-mode MCFs, where the rotational misalignment is assumed to be 0.5 degree without transverse offset.

the channel density per unit area normalized by that of the standard SMF, and hexagonally arranged 3, 7, 12, 19, and 27 cores are assumed. The spatial density is drastically increased by increasing the number of modes in each core. Thus, it is preferable to increase the number of modes in each core than increase the number of cores. Because when the number of modes in each core is kept constant and the number of cores is increased, the spatial density (channel density per unit area) is almost unchanged under the condition that the core-to-core distance is constant (XT level is kept constant). Fig. 19 indicates that about 50 times larger spatial density can be achieved compared with that of the SMF under a condition of CD < 250 μm using a 9LP-mode 12-core fiber with a channel count of 180. In theory, a further increase in spatial density is possible by increasing the number of modes M and/or cores N; however, the mode dependent loss (MDL) degradation at a splicing point will be problematic [30] because of the rotational misalignment.

In MCF splicing, the rotational misalignment angle is 0.6 degree on average [34], which results in different values of the offset for the inner and outer cores. Fig. 20 shows the numerically
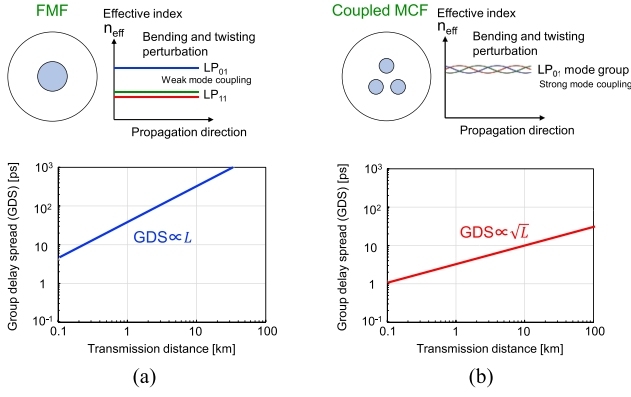
Fig. 21. Mode mixing and GDS in (a) a single-core FMF and (b) a coupled MCF.

evaluated maximum MDL at a splicing point at $\lambda = 1550$ nm as a function of number of cores for 2LP-, 4LP-, 6LP-, and 9LP-mode MCFs, wherein the rotational misalignment is assumed to be 0.5 degree without the transverse offset and the fiber parameters are listed in Tables II and III. The MDL is evaluated using the complex transmission matrix $\boldsymbol{T}_c$ between the input mode field vector ϕ_{in} and the output mode field vector ϕ_{out} at the splicing point, where $\phi_{out} = \boldsymbol{T}_c \phi_{in}$. The MDL (in dB unit) is defined as

$$MDL = 20 \log_{10} \left(\lambda_{max} / \lambda_{min} \right), \quad (28)$$

where λ_{max} and λ_{min} represent the maximum and minimum singular values of $\boldsymbol{T}_c$ obtained by singular value decomposition [35]. Fig. 20 indicates that the maximum MDL for the 2LP-mode MCF is moderately small; however, the MDL reaches an unacceptable level when the number of modes is increased. Therefore, for long distance transmission using uncoupled few-mode MCFs where each core supports several different spatial modes, the mitigation of MDL degradation at the splicing point is expected to become an important technology.

IV. COUPLING MECHANISMS IN COUPLED MCFS

A. Coupled Mode Theory for Modal Group Delay Analysis

Coupled MCFs are considered a type of few-mode/multi-mode fibers. In multi-mode transmission, the complexity of MIMO DSP is proportional to the group delay spread (GDS) attributed to modal dispersion [36], and therefore GDS reduction is highly required. The GDS in single-core FMFs increases in proportion to the transmission distance, which results in the limitation of the transmission distance or number of modes. The GDS in the coupled MCFs with the strong mode mixing state is proportional to the square root of the transmission distance [37], which allows the long-distance mode-division multiplexing (MDM) transmission. The strong mode mixing in coupled MCFs was first reported in [8], and several long-distance MDM transmission experiments using coupled MCFs have been reported since then [38]–[43].

Fig. 21 shows the difference between a single-core FMF and a coupled MCF. In the single-core FMF, as shown in Fig. 21(a), the difference in the effective index, n_{eff}, between different

mode groups is large and does not change along the propagation direction even if the fiber has bending and twisting perturbations. Therefore, mode coupling between different mode groups is not strong, and this results in a linear increase in the GDS with an increase in the propagation distance. In the coupled MCF, as shown in Fig. 21(b), the difference in the n_{eff} between coupled modes is small and changes along the propagation direction if the fiber has bending and twisting perturbations. Then, mode coupling between the coupled modes becomes strong, and group delays in different modes are averaged, which results in a GDS increase proportional to the square root of the propagation distance.

The mode mixing and GDS in coupled MCFs can be evaluated by CMT. The coupled mode equation for the waveguide mode system with the number of modes of N (e.g., single-mode coupled N cores) is expressed as [44]

$$\frac{da_n(z)}{dz} = -j\beta_n(z) a_n(z) - j \sum_{m \neq n}^{N} \kappa_{nm}(z) a_m(z), \quad (29)$$

where $a_n(z)$ and $\beta_n(z)$ represent the complex mode amplitude and propagation constant of the n-th guided mode, and $\kappa_{nm}(z)$ denotes the coupling coefficient between the n-th and m-th guided modes. Not only the field amplitude but also the phase must be fully considered for treating the change in the modal group delay attributed to perturbations [45]. The solution of (29) after the propagation of distance z is given using a column vector $\boldsymbol{a}(z)$ as

$$\boldsymbol{a}(z) = \begin{bmatrix} a_1(z) \\ \vdots \\ a_N(z) \end{bmatrix} = \boldsymbol{T}(\omega) \boldsymbol{a}(0), \quad (30)$$

where $\boldsymbol{T}(\omega)$ denotes the total transmission matrix and ω represents the angular frequency. Using $\boldsymbol{T}(\omega)$, the group delay operator $\boldsymbol{GDO}(\omega)$ is defined by [46]

$$\boldsymbol{GDO}(\omega) = j\boldsymbol{T}(\omega)^{-1} \frac{d\boldsymbol{T}(\omega)}{d\omega}, \quad (31)$$

and GDS is expressed using the eigenvalue of $\boldsymbol{GDO}(\omega)$ as [47], [48]

$$GDS = \sqrt{\frac{1}{N} \sum_{i=1}^{N} \tau_i^2}, \quad (32)$$

where τ_i represents the i-th eigenvalue of $\boldsymbol{GDO}(\omega)$ and is normalized as $\sum \tau_i = 0$. The derivative of the total transmission matrix with respect to the angular frequency in (31) is numerically calculated by

$$\frac{d\boldsymbol{T}(\omega)}{d\omega} \approx \frac{\boldsymbol{T}(\omega + \Delta\omega) - \boldsymbol{T}(\omega - \Delta\omega)}{2\Delta\omega}, \quad (33)$$

where $\Delta\omega$ represents a sufficiently small angular frequency difference from the central ω. The fiber length L is divided into small segments of length ΔL to obtain the total transmission matrix $\boldsymbol{T}(\omega)$ considering structural perturbations. If ΔL is sufficiently small, the structure can be assumed to be uniform in each segment, and in each segment, Eq. (29) can be re-written
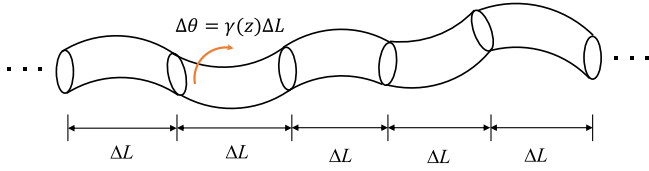
Fig. 22. Schematic of the perturbation of $\Delta\theta$ applied in each segment, where ΔL denotes the segment length.

as

$$\frac{d\boldsymbol{a}(z)}{dz} = -j \begin{bmatrix} \beta_1 & \kappa_{12} & \dots & \kappa_{1N} \\ \kappa_{21} & \beta_2 & & \kappa_{2N} \\ \vdots & & \ddots & \vdots \\ \kappa_{N1} & \dots & \kappa_{NN-1} & \beta_N \end{bmatrix} \boldsymbol{a}(z)$$

$$= -j\boldsymbol{C}^{-1} \begin{bmatrix} \tilde{\beta}_1 & 0 & \dots & 0 \\ 0 & \tilde{\beta}_2 & & 0 \\ \vdots & & \ddots & \vdots \\ 0 & \dots & 0 & \tilde{\beta}_N \end{bmatrix} \boldsymbol{C}\boldsymbol{a}(z), \qquad (34)$$

where β_n represents the propagation constant of the coupled core mode (super-mode), $\tilde{\beta}_n$ denotes the propagation constant of the discrete core mode, and the matrix $\boldsymbol{C}$ represents the butt coupling coefficient matrix between the discrete core mode and coupled core mode. $\tilde{\beta}_n$ is randomly perturbed in each segment and changes to $\tilde{\beta}'_n$ by considering structural perturbations such as bending and twisting, which is given as

$$\tilde{\beta}'_n(z) = \tilde{\beta}_n \left[1 + \frac{D_n}{R(z)} \cos\{\theta_n(z)\} \right], \qquad (35)$$

where D_n represents the distance from the fiber center to the core center of Core n, $R(z)$ denotes the bending radius in the fiber at the z position, and $\theta_n(z)$ represents the twisting angle in Core n at the z position. The perturbation of $\tilde{\beta}'_n(z)$ results in the coupling coefficient perturbation, which enhances mode coupling between different modes. Therefore, the larger the perturbation, the more enhanced is the mode mixing in the coupled MCFs.

$R(z)$ and $\theta_n(z)$ in each segment are expressed as

$$R(z + \Delta L) = R(z) + \Delta R(z), \qquad (36)$$

$$\theta_n(z + \Delta L) = \theta_n(z) + \Delta\theta(z), \qquad (37)$$

where $\Delta R(z)$ and $\Delta\theta(z)$ represent the bending radius change and twisting angle change from the previous segment, respectively. In the following, $R(z)$ is assumed to be constant bending radius of R and $\Delta R(z) = 0$, for simplicity. If the R is sufficiently small to induce a strong mode mixing, there is no essential difference in the averaged GDS with or without considering the random $\Delta R(z)$ for $\Delta R(z) \ll R$ [49]. For $\Delta\theta(z)$, it is assumed that each segment has randomly generated twisting rate $\gamma(z)$ and the twisting angle $\Delta\theta(z)$ relative to the previous segment is given by $\gamma(z)\Delta L$ as shown in Fig. 22. Further, $\gamma(z)$ is assumed to have Gaussian distribution with the mean value of γ_{ave} and the standard deviation of σ_γ, wherein $\gamma(z)$ is constant in each segment and it changes from segment to segment. The introduction of the random twisting rate is not
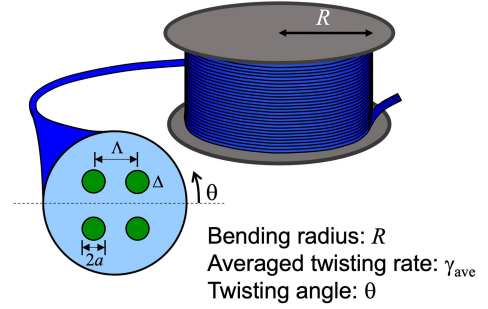

Fig. 23. Schematic of coupled 4-core fiber with the bending radius R, where the twist rate γ is assumed to change randomly following a normal distribution with the mean value γ_{ave} and standard deviation σ_γ.
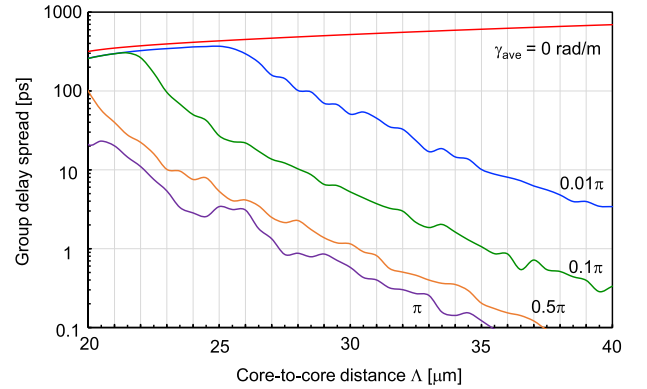

Fig. 24. GDS after 1 km propagation as a function of core-to-core distance Λ in a coupled 4-core fiber with $a = 4.5$ μm, $\Delta = 0.35\%$, and $R = 140$ mm for several different values of γ_{ave}, where the standard deviation of twist rate following a normal distribution is $\sigma_\gamma = 0.01$ rad/m.

mandatory for GDS evaluation; however, if the twisting rate is constant, there will be eigen states propagating in a uniformly twisting waveguide. The weak random twisting is considered to avoid such unrealistic states. The accuracy of the final solution of (34) depends on the size of ΔL, and to obtain a reasonably converged value of the averaged GDS, $\Delta L = 0.1$ mm is used hereafter.

B. Group Delay Spread in Coupled MCFs

As an example, the GDS change attributed to twisting perturbation in a coupled 4-core fiber with the constant R as shown in Fig. 23 is considered, wherein the core radius is a, the relative refractive index difference between core and cladding is Δ, and the core-to-core distance is Λ. Fig. 24 shows the GDS after 1 km propagation as a function of Λ in the coupled 4-core fiber with $a = 4.5$ μm, $\Delta = 0.35\%$, and $R = 140$ mm for several different values of γ_{ave}, wherein the $\sigma_\gamma = 0.01$ rad/m and the GDS is calculated from the average of 100 calculation results at $\lambda = 1550$ nm. When the averaged twisting rate γ_{ave} is 0, the GDS is several hundred picoseconds, whereas the GDS is decreased with an increase in the averaged twisting rate. The increment in the twisting perturbation results in a decrement in the modal dispersion. In Fig. 24, we assume that all cores have the same core parameters, and therefore, the GDS is decreased with an increase in the core-to-core distance. This is an ideal case, but it
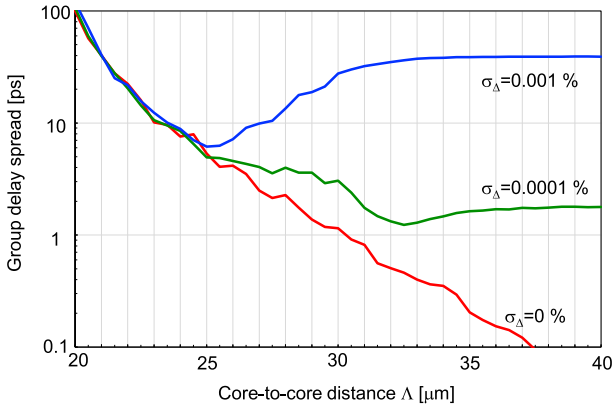
Fig. 25. GDS after 1 km propagation as a function of core-to-core distance Λ in a coupled 4-core fiber with small fabrication error in each core, where $a = 4.5$ μm, $\Delta_{\mathrm{ave}} = 0.35\%$, $R = 140$ mm, $\gamma_{\mathrm{ave}} = 0.5\pi$ rad/m, and $\sigma_{\gamma} = 0.01$ rad/m.

Fig. 26. GDS in coupled 4-core fibers as a function of propagation distance for $\Lambda = 25$ μm and 35 μm, where $a = 4.5$ μm, $\Delta_{\mathrm{ave}} = 0.35\%$, $\sigma_{\Delta} = 0.001\%$, and $R = 140$ mm.

Fig. 27. GDS dependence on core parameters in coupled 4-core fibers, where $a = 4.5$ μm, $\gamma_{\mathrm{ave}} = 0.5\pi$ rad/m, $\sigma_{\gamma} = 0.01$ rad/m, and $R = 140$ mm. The blue, red, and green curves represent the GDS results after 1 km propagation for the averaged core Δ of $\Delta_{\mathrm{ave}} = 0.3\%$, 0.35%, and 0.39%, respectively, wherein the standard deviation of random core Δ error is assumed to be $\sigma_{\Delta} = 0.001\%$.

is not realistic. In addition, Fig. 24 does not clarify the location of the weak or strong mode coupling region.

Next, a coupled 4-core fiber with small fabrication error in each core is considered, wherein each core is assumed to have the core Δ following a normal distribution with the mean value of Δ_{ave} and standard deviation σ_{Δ}. Fig. 25 shows the GDS after 1 km propagation as a function of the core-to-core distance in the coupled 4-core fiber with $a = 4.5$ μm, $\Delta_{\mathrm{ave}} = 0.35\%$, $R = 140$ mm, $\gamma_{\mathrm{ave}} = 0.5\pi$ rad/m, and $\sigma_{\gamma} = 0.01$ rad/m. The GDS is calculated from the average of 100 calculation results at $\lambda = 1550$ nm. The red, green, and blue curves represent the results for $\sigma_{\Delta} = 0, 0.0001$, and 0.001%, respectively. Assuming a very small core Δ error of $\sigma_{\Delta} = 0.001\%$, the GDS curve is minimal at a core-to-core distance of about 25 μm and the GDS cannot be lower than a few picoseconds. This is because when the core-to-core distance Λ is larger than 30 μm, the mode mixing effect is weak and the GDS is dominated by the difference in the group index between the cores attributed to the difference in the introduced intrinsic core Δ. In this case, it cannot be used as a coupled MCF. Further, if Λ is less than about 20 μm, the GDS is dominated by the group delay difference between the super-modes of the coupled cores, and the fiber is used as a conventional multimode fiber such as a single-core FMF. When Λ is set moderately, e.g., $\Lambda = 25$ μm, the GDS is reduced by the strong mode mixing effect. This appropriate core-to-core distance is slightly changed by the twisting rate. The GDS tends to decrease and the appropriate core-to-core distance shifts to the smaller side when the twisting rate is increased. When the twisting rate is decreased the GDS tends to increase and the appropriate core-to-core distance shifts to the larger side. Fig. 26 shows the GDS in the coupled 4-core fibers as a function of propagation distance at $\lambda = 1550$ nm, where $a = 4.5$ μm, $\Delta_{\mathrm{ave}} = 0.35\%$, $\sigma_{\Delta} = 0.001\%$, $\gamma_{\mathrm{ave}} = 0.5\pi$ rad/m, and $R = 140$ mm. Red and blue lines are results for $\Lambda = 25$ μm and 35 μm, respectively. The red line is roughly proportional to the square root of propagation distance L after several kilometers of propagation, wherein the black dashed line is a fitting line of $\sqrt{L}$-proportion behavior. The blue line shows a linear increase
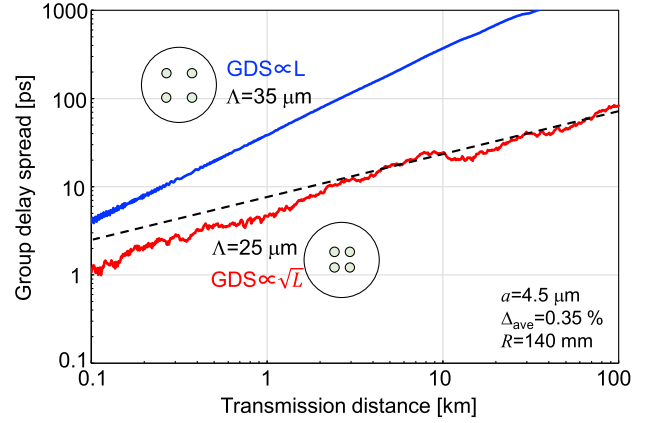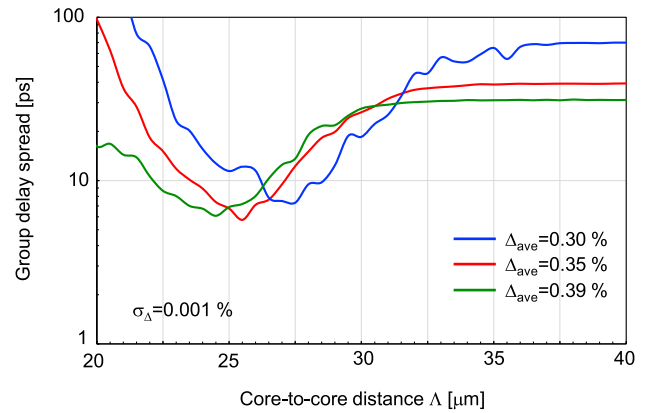
with propagation distance. This result indicates the core-to-core distance in the coupled MCFs must be appropriately selected to enhance the mode mixing effect [50]–[52].

If fiber parameters are fixed, changing the averaged bending condition R does not change the appropriate (optimal) core-to-core distance for strong mode mixing; instead, the optimal core-to-core distance can be shifted by changing the core parameters and/or the core index profile. Fig. 27 shows the GDS dependence on the core parameters in coupled 4-core fibers, wherein $a = 4.5$ μm, $\gamma_{\mathrm{ave}} = 0.5\pi$ rad/m, $\sigma_{\gamma} = 0.01$ rad/m, and $R = 140$ mm. The blue, red, and green curves represent the GDS results after 1 km propagation for the averaged core Δ of $\Delta_{\mathrm{ave}} = 0.3\%$, 0.35%, and 0.39%, respectively, wherein the standard deviation of the random core Δ error is assumed to be $\sigma_{\Delta} = 0.001\%$. The optimal core-to-core distance for the strong mode mixing is shifted by changing the core parameters, and it can be decreased by increasing the normalized frequency (V-parameter).

Thus far, the bending radius of the fiber is fixed at $R = 140$ mm for the GDS evaluation as an example; however, the GDS depends on the bending conditions. Fig. 28 shows the
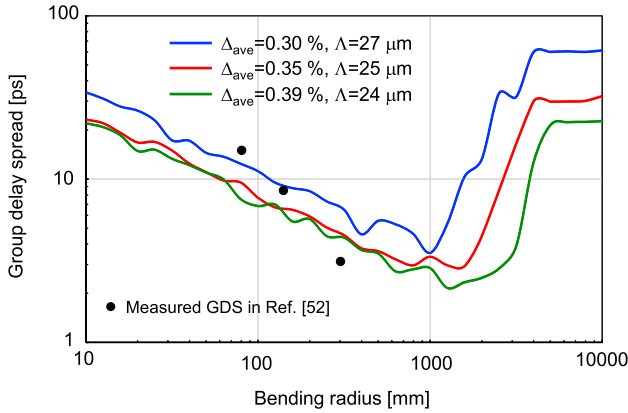
Fig. 28. GDS dependence on the bending radius R in coupled 4-core fibers, where $a = 4.5$ μm, $\gamma_{ave} = 0.5\pi$ rad/m, and $\sigma_\gamma = 0.01$ rad/m. The blue, red, and green curves represent the GDS results after 1 km propagation for the averaged core Δ of $\Delta_{ave} = 0.3\%$, 0.35%, and 0.39%, respectively, wherein the standard deviation of random core Δ error is assumed to be $\sigma_\Delta = 0.001\%$.

GDS dependence on the bending radius R in coupled 4-core fibers, wherein $a = 4.5$ μm, $\gamma_{ave} = 0.5\pi$ rad/m, and $\sigma_\gamma = 0.01$ rad/m. The blue, red, and green curves represent the GDS results after 1 km propagation for the averaged core Δ of $\Delta_{ave} = 0.3\%$, 0.35%, and 0.39%, respectively, wherein the standard deviation of random core Δ error is assumed to be $\sigma_\Delta = 0.001\%$. For $\Delta_{ave} = 0.3\%$, 0.35%, and 0.39%, the core-to-core distance is set to $\Lambda = 27$ μm, 25 μm, and 24 μm, respectively, as the optimum values for the enhancing mode mixing. GDS decreases with an increase in the R up to about 1000 mm. The black circle plots represent the reported measured GDS in a coupled 4-core fiber for three different bending sizes [52]; they have a similar tendency with the numerically evaluated results. Further, the GDS is quickly increased when the bending radius is too large. Because when the effective index variation attributed to the bending perturbations is larger than the effective index difference between different modes, a larger bending radius is preferable to reduce the averaged group delay difference between different mode, which results in the GDS reduction for a larger bending radius. When the bending radius is too large, the bending perturbations do not induce mode mixing, which results in a quick increase in the modal dispersion for a larger bending radius. From these results, it is estimated that the minimum achievable GDS in the coupled MCFs without intentional twisting control will be about a few ps/$\sqrt{\text{km}}$.

The GDS may be controlled by changing the number of cores in the coupled MCFs. Therefore, the GDS dependence on the number of cores in coupled MCFs is considered. Fig. 29 shows the GDS dependence on the number of cores in coupled MCFs with core-to-core distances of 20 μm, 22 μm, and 24 μm after 1 km propagation, wherein $a = 4.5$ μm, $\Delta_{ave} = 0.35\%$, $\sigma_\Delta = 0.001\%$, $\gamma_{ave} = 0.5\pi$ rad/m, $\sigma_\gamma = 0.01$ rad/m, and $R = 140$ mm. The GDS is calculated from the average of 100 calculation results at $\lambda = 1550$ nm. Fig. 29 indicates that if the core-to-core distance is the same, the level of GDS does not change considerably regardless of the number of cores because even if the number of cores is changed, the core-to-core distance remains
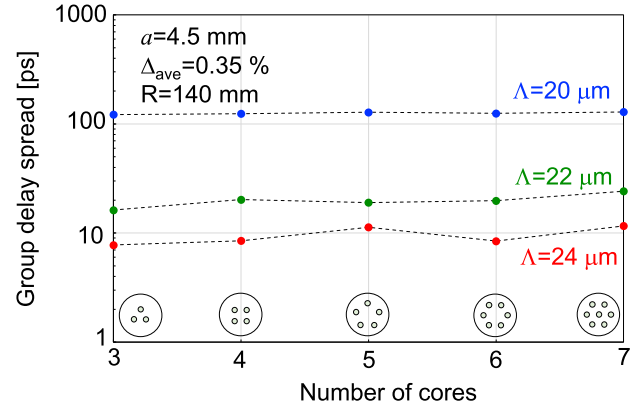

Fig. 29. GDS dependence on the number of cores in the coupled MCFs with core-to-core distances of 20 μm, 22 μm, and 24 μm after 1 km propagation, wherein $a = 4.5$ μm, $\Delta_{ave} = 0.35\%$, $\sigma_\Delta = 0.001\%$, $\gamma_{ave} = 0.5\pi$ rad/m, $\sigma_\gamma = 0.01$ rad/m, and $R = 140$ mm.
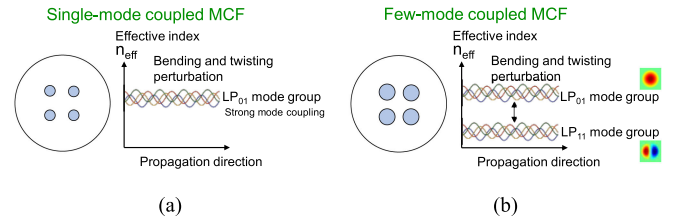

Fig. 30. Comparison of the effective index variation caused by bending and twisting perturbations in (a) a single-mode coupled MCF and (b) a few-mode coupled MCF, where each core in the few-mode coupled MCF is assumed to support two LP modes, LP_{01} and LP_{11}.

the same, and the maximum effective index difference between the nearest non-degenerated modes becomes similar. Therefore, a drastic GDS change is not expected when changing the number of cores in the coupled MCFs with a fixed core-to-core distance.

V. POSSIBILITY FOR FEW-MODE COUPLED MCFs

When each core of a coupled MCF is a single-mode core, the GDS can be reduced by setting the core-to-core distance appropriately. However, if each core of a coupled MCF is a multi-mode core, it becomes difficult to achieve strong mode mixing. Fig. 30 shows a comparison of the effective index variation attributed to bending and twisting perturbations in a single-mode coupled MCF and a few-mode coupled MCF, wherein each core in the few-mode coupled MCF is assumed to support two LP modes of LP_{01} and LP_{11} modes. In the 2LP-mode coupled MCF, LP_{01} mode group and LP_{11} mode group exist as shown in Fig. 30(b). In the same mode group, strong mode mixing can be obtained by gentle bending perturbation, which is the same as in the single-mode coupled MCF. A large bending perturbation is required to enhance mode coupling between different mode groups because the effective index difference between different mode groups is considerably larger than that between modes in the same mode group. Further, the group velocity of the LP_{01} mode group and that of LP_{11} mode group are different, and therefore, strong mode mixing is not obtained even if strong bending perturbation is introduced. Therefore, in coupled few-mode MCFs, the following two conditions need to be satisfied for
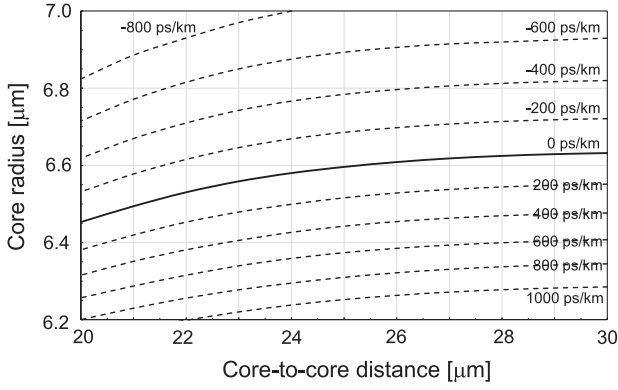
Fig. 31. Averaged DMGD along the propagation direction between the LP_{01} and LP_{11} mode groups in a bent and twisted 2LP-mode coupled 4-core fiber as functions of core-to-core distance and core radius, where $\Delta = 0.3\%$ and $R = 100$ mm.
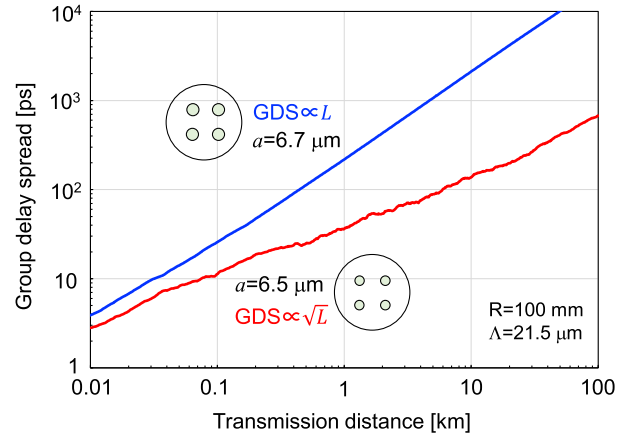

Fig. 32. GDS at $\lambda = 1550$ nm for the 2LP-mode coupled 4-core fiber as a function of the propagation distance, where $\Lambda = 21.5\ \mu$m, $\Delta = 0.3\%$, $\gamma_{ave} = 0.5\pi$ rad/m, $\sigma_\gamma = 0.01$ rad/m, and $R = 100$ mm.
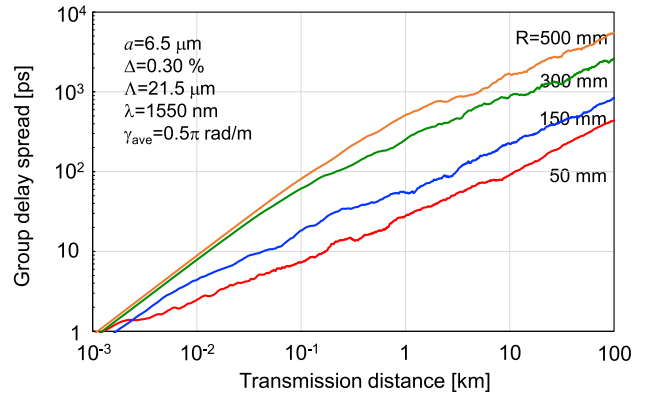

Fig. 33. GDS in the 2LP-mode coupled 4-core fiber as a function of the propagation distance for $R = 50$, 150, 300, and 500 mm, where $a = 6.5\ \mu$m, $\Delta = 0.3\%$, $\Lambda = 21.5\ \mu$m, $\gamma_{ave} = 0.5\pi$ rad/m, $\sigma_\gamma = 0.01$ rad/m, and $\lambda = 1550$ nm.

strong mode mixing. The first one is strong bending perturbation, which indicates the tight bending condition. The second one is that all mode groups should have similar group velocity, namely averaged DMGD between different mode groups should be low. For 2LP-mode N-core fiber, the averaged DMGD ($DMGD_{ave}$) is given by

$$DMGD_{ave} = \frac{1}{c} \left(\frac{1}{N} \sum_{i=1}^{N} n_{gave,i} - \frac{1}{2N} \sum_{i=N+1}^{3N} n_{gave,i} \right), \tag{38}$$

where c denotes the speed of light in vacuum and $n_{gave,i}$ represents the averaged group index of the i-th super-mode along the propagation direction under the bending and twisting perturbation. The first term on the right side in (38) represents the averaged group delay of the LP_{01} mode group per unit length and the second term represents that of the LP_{11} mode group. $n_{gave,i}$ can be obtained by averaging the group index over one twisting period with constant R, and it is obtained by

$$n_{gave,i} = \frac{1}{l_\gamma} \int_z^{z+l_\gamma} n_{g,i}(z)\, dz, \tag{39}$$

where $n_{g,i}(z)$ denotes the group index of the i-th super-mode at the z position and l_γ represents the twisting period. $n_{g,i}(z)$ is numerically calculated by using FEM [31].

Fig. 31 shows the averaged DMGD along the propagation direction between the LP_{01} and LP_{11} mode groups in a bent and twisted 2LP-mode coupled 4-core fiber as functions of core-to-core distance and core radius, respectively, wherein the refractive index profile is assumed to be a step index with a core Δ of 0.3% as an example and $R = 100$ mm. The black solid line represents $DMGD_{ave} = 0$ ps/km and the dashed contour lines are 200 ps/km intervals. In the bent and twisted 2LP-mode 4-core fiber, the averaged DMGD can be reduced by appropriately setting the core-to-core distance and core radius. The low GDS is expected in the 2LP-mode coupled 4-core fiber with a tight bending perturbation when using the low DMGD region. In Fig. 31, a step-index profile in each core is assumed as an example. One can expect that a graded-index profile in each core can be used for controlling DMGD between the coupled LP_{01} and LP_{11} mode groups [53]. However, in the case of strong bending perturbation, fine control of index-α value in each

core does not have any considerable impact. Fig. 32 shows the numerically calculated GDS at $\lambda = 1550$ nm for the 2LP-mode coupled 4-core fiber as a function of the propagation distance, where the core-to-core distance $\Lambda = 21.5\ \mu$m, $\Delta = 0.3\%$, $\gamma_{ave} = 0.5\pi$ rad/m, $\sigma_\gamma = 0.01$ rad/m, and $R = 100$ mm. The blue and red lines represent results for the core radius of 6.7 μm and 6.5 μm, respectively. The red line is roughly proportional to the square root of the propagation distance, whereas the blue line increases linearly with an increase in the propagation distance. These results indicate that the core parameters (a, Δ) and core-to-core distance need to be carefully determined to enhance mode mixing for all modes.

Finally, the GDS in the 2LP-mode coupled 4-core fiber as a function of the propagation distance for some different bending conditions is shown in Fig. 33 to confirm the effect of the amount of bending perturbation on the mode mixing, where $a = 6.5\ \mu$m, $\Delta = 0.3\%$, $\Lambda = 21.5\ \mu$m, $\gamma_{ave} = 0.5\pi$ rad/m, $\sigma_\gamma = 0.01$ rad/m, and $\lambda = 1550$ nm. A tight bending condition is preferable in few-mode coupled MCFs to introduce strong bending perturbation, which results in strong mode mixing between the different mode groups. In actual fiber cables, the bending condition is

not constant; however, a low GDS few-mode coupled MCF is realized if the averaged bending condition can be controlled in a cable. Recently, a controlling technology of the bending condition in a fiber cable has been reported [54] for reducing the GDS in coupled MCFs, and by using this approach, few-mode coupled MCFs with low GDS in actual fiber cables will be achieved.

VI. CONCLUSION

Coupling mechanisms in uncoupled and coupled MCFs for SDM transmission have been described using CMT. For designing uncoupled MCFs, random structural fluctuations can be considered by introducing random phase noise and/or random polarization mode coupling. In uncoupled MCFs, when the bending perturbation is dominant, i.e., phase matching between neighboring cores randomly occurs many times along the propagation direction, the averaged inter-core *XT* is determined by the coupling coefficient between cores, whereas when the bending perturbation is weak, random structural fluctuations play an important role in determining the *XT*, and the randomness should be reduced for decreasing *XT*. The transmission capacity can be increased by two orders of magnitude by combining mode and core multiplexing in uncoupled MCFs; however, the degradation of mode dependent characteristics at the splicing point must be mitigated. Further, in coupled MCFs, the core-to-core distance need to be carefully determined to enhance mode mixing. Larger structural perturbations result in lower modal dispersions in the coupled MCFs. Strong mode mixing is relatively easily obtained in single-mode coupled MCFs; however, in few-mode coupled MCFs with bending and twisting perturbations, two design conditions, i.e., the smaller bending size of the cable and the lower averaged DMGD between different mode groups, are required for strong mode mixing. The development of few-mode coupled MCFs with high SDM channels and low GDS will enable extreme SDM fibers with high spatial density for large capacity long distance transmissions.

Finally, after the proposal of MCFs for overcoming the expected capacity crunch of conventional SMFs [2], it has now been over 10 years and research on MCFs have been moving from the R&D stage to the practical application stage. The application area in near future will be expected to relatively short distance (less than 100 km) point-to-point transmission without using optical amplifiers, such as, data centers and interconnections. In this stage, the development of a lower cost system is highly desired in comparison with the parallel SMF transmission system. Then, the other application area would be long-distance transmission with an efficient optical amplifier, such as in a submarine system. In further long-term range, MCFs are expected to be installed on terrestrial network to replace SMFs, and at this stage, international standardization regarding MCFs in addition to economic benefits will be desired.

REFERENCES

[1] R.-J. Essiambre, G. Kramer, P. J. Winzer, G. J. Foschini, and B. Goebel, "Capacity limits of optical fiber networks," *J. Lightw. Technol.*, vol. 28, no. 4, pp. 662–701, Feb. 2010.

[2] T. Morioka, Y. Awaji, R. Ryf, D. Richardson, and F. Poletti, "Enhancing optical communications with brand new fibers," *IEEE Commun. Mag.*, vol. 50, no. 2, pp. S31–S42, Feb. 2012.

[3] P. Sillard, M. Bigot-Astruc, and D. Molin, "Few-mode fibers for mode-division-multiplexed systems," *J. Lightw. Technol.*, vol. 32, no. 16, pp. 2824–2829, Aug. 2014.

[4] D. Soma, Y. Wakayama, K. Igarashi, and T. Tsuritani, "Partial MIMO-based 10-mode-multiplexed transmission over 81 km weakly-coupled few-mode fiber," in *Proc. Opt. Fiber Commun. Conf.*, Los Angeles, CA, USA, 2017, Art. no. MD2.4.

[5] R. Ryf *et al.*, "High-spectral-efficiency mode-multiplexed transmission over graded-index multimode fiber," in *Proc. Eur. Conf. Opt. Commun.*, Rome, Italy, 2018, Art. no. Th3B.1.

[6] T. Hayashi, T. Taru, O. Shimakawa, T. Sasaki, and E. Sasaoka, "Design and fabrication of ultra-low crosstalk and low-loss multi-core fiber," *Opt. Express*, vol. 19, no. 17, pp. 16576–16592, Aug. 2011.

[7] J. Sakaguchi *et al.*, "19-core fiber transmission of 19x100x172-Gb/s SDM-WDM-PDM-QPSK signal at 305 Tb/s," in *Proc. Opt. Fiber Commun. Conf.*, Los Angeles, CA, USA, 2012, Art. no. PDP5C.1.

[8] R. Ryf *et al.*, "Coherent 1200-km 6x6 MIMO mode-multiplexed transmission over 3-core microstructured fiber," in *Proc. Eur. Conf. Opt. Commun.*, Geneva, Switzerland, 2011, Art. no. Th.13.C.1.

[9] T. Sakamoto *et al.*, "120 spatial channel few-mode multi-core fibre with relative core multiplicity factor exceeding 100," in *Proc. Eur. Conf. Opt. Commun.*, Rome, Italy, 2018, Art. no. We3E.3.

[10] M. Koshiba, K. Saitoh, K. Takenaga, and S. Matsuo, "Multi-core fiber design and analysis: Coupled-mode theory and coupled-power theory," *Opt. Express*, vol. 19, no. 26, pp. B102–B111, Dec. 2011.

[11] A. W. Snyder and J. D. Love, *Optical Waveguide Theory*, London, U.K: Chapman and Hall, 1983.

[12] T. Hayashi, T. Nagashima, O. Shimakawa, T. Sasaki, and E. Sasaoka, "Crosstalk variation of multi-core fiber due to fiber bend," in *Proc. Eur. Conf. Opt. Commun.*, Torino, Italy, 2010, Art. no. We.8.F.6.

[13] A. V. T. Cartaxo and J. A. P. Morgado, "New expression for evaluating the mean crosstalk power in weakly-coupled multi-core fibers," *J. Lightw. Technol.*, vol. 39, no. 6, pp. 1830–1842, Mar. 2021.

[14] M. Koshiba, K. Saitoh, K. Takenaga, and S. Matsuo, "Analytical expression of averaged power-coupling coefficients for estimating intercore crosstalk in multicore fibers," *IEEE Photon. J.*, vol. 4, no. 5, pp. 1987–1995, Oct. 2012.

[15] T. Hayashi, T. Taru, O. Shimakawa, T. Sasaki, and E. Sasaoka, "Characterization of crosstalk in ultra-low-crosstalk multi-core fiber," *J. Lightw. Technol.*, vol. 30, no. 4, pp. 583–589, Feb. 2012.

[16] A. V. T. Cartaxo and T. M. F. Alves, "Discrete changes model of inter-core crosstalk of real homogeneous multi-core fibers," *J. Lightw. Technol.*, vol. 35, no. 12, pp. 2398–2408, Jun. 2017.

[17] T. M. F. Alves, R. O. J. Soeiro, and A. V. T. Cartaxo, "Probability distribution of intercore crosstalk in weakly coupled MCFs with multiple interferers," *IEEE Photon. Technol. Lett.*, vol. 31, no. 8, pp. 651–654, Apr. 2019.

[18] R. O. J. Soeiro, T. M. F. Alves, and A. V. T. Cartaxo, "Dual polarization discrete changes model of inter-core crosstalk in multi-core fibers," *IEEE Photon. Technol. Lett.*, vol. 29, no. 16, pp. 1395–1398, Aug. 2017.

[19] C. Antonelli, G. Riccardi, T. Hayashi, and A. Mecozzi, "Role of polarization-mode coupling in the crosstalk between cores of weakly-coupled multi-core fibers," *Opt. Express*, vol. 28, no. 9, pp. 12847–12861, Apr. 2020.

[20] P. K. A. Wai and C. R. Menyuk, "Polarization decorrelation in optical fibers with randomly varying birefringence," *Opt. Lett.*, vol. 19, no. 19, pp. 1517–1519, Oct. 1994.

[21] Y. Amma, K. Takenaga, T. Fujisawa, K. Saitoh, M. Koshiba, and K. Aikawa, "Dependence of cladding diameter on inter-core crosstalk in heterogeneous multi-core fibers," in *Proc. Optoelectron. Commun. Conf.*, Jeju, Korea, 2018, Art. no. 3C2-2.

[22] Y. Amma *et al.*, "High-density multicore fiber with heterogeneous core arrangement," in *Proc. Opt. Fiber Commun. Conf.*, Los Angeles, CA, USA, 2015, Art. no. Th4C.4.

[23] C. Antonelli, T. Hayashi, and A. Mecozzi, "Random polarization-mode coupling explains inter-core crosstalk in uncoupled multi-core fibers," in *Proc. Eur. Conf. Opt. Commun.*, Brussels, Belgium, 2020, Art. no. Th1A-1.

[24] K. Takenaga *et al.*, "A large effective area multi-core fiber with an optimized cladding thickness," *Opt. Express*, vol. 19, no. 26, pp. B542–B550, Dec. 2011.

[25] S. Matsuo *et al.*, "Large-effective-area ten-core fiber with cladding diameter of about 200 μm," *Opt. Lett.*, vol. 36, no. 23, pp. 4626–4628, Dec. 2011.

[26] K. Shibahara *et al.*, "Dense SDM (12-core × 3-mode) transmission over 527 km with 33.2-ns mode-dispersion employing low-complexity parallel MIMO frequency-domain equalization," in *Proc. Opt. Fiber Commun. Conf.*, Los Angeles, CA, USA, 2015, Art. no. Th5C.3.

[27] T. Sakamoto *et al.*, "Few-mode multi-core fibre with highest core multiplicity factor," in *Proc. Eur. Conf. Opt. Commun.*, Valencia, Spain, 2015, Art. no. We.1.4.3.

[28] T. Sakamoto *et al.*, "Low-loss and low-DMD few-mode multi-core fiber with highest core multiplicity factor," in *Proc. Opt. Fiber Commun. Conf.*, Anaheim, CA, USA, 2016, Art. no. Th5A.2.

[29] T. Sakamoto *et al.*, "High spatial density six-mode seven-core fibre for repeated dense SDM transmission," in *Proc. Eur. Conf. Opt. Commun.*, Gothenburg, Sweden, 2017, Art. no. Th.PDP.A.6.

[30] T. Sakamoto *et al.*, "Spatial density and splicing characteristic optimized few-mode multi-core fiber," *J. Lightw. Technol.*, vol. 38, no. 16, pp. 4490–4496, Aug. 2020.

[31] K. Saitoh and M. Koshiba, "Full-vectorial imaginary-distance beam propagation method based on a finite element scheme: Application to photonic crystal fibers," *IEEE J. Quantum Electron.*, vol. 38, no. 7, pp. 927–933, Jul. 2002.

[32] Y. Sasaki, K. Takenaga, S. Matsuo, K. Aikawa, and K. Saitoh, "Few-mode multicore fibers for long-haul transmission line," *Opt. Fiber Technol.*, vol. 35, pp. 19–27, Feb. 2017.

[33] P. J. Winzer, A. H. Gnauck, A. Konczykowska, F. Jorge, and J.-Y. Dupuy, "Penalties from in-band crosstalk for advanced optical modulation formats," in *Proc. Eur. Conf. Opt. Commun.*, Geneva, Switzerland, 2011, Art. no. Tu.5.B.7.

[34] Y. Amma, A. Takahashi, K. Takenaga, and S. Matsuo, "Accuracy of core alignment with end-view function for multicore fiber," in *Proc. IEEE Photon. Soc. Summer Topical Meeting*, Montreal, QC, Canada, 2014, Art. no. TuE2.1.

[35] M. Shirata, T. Fujisawa, T. Sakamoto, T. Matsui, K. Nakajima, and K. Saitoh, "Design of small mode-dependent-loss scrambling-type mode (de)multiplexer based on PLC," *Opt. Express*, vol. 28, no. 7, pp. 9653–9665, Mar. 2020.

[36] B. Inan *et al.*, "DSP complexity of mode-division multiplexed receivers," *Opt. Express*, vol. 20, no. 9, pp. 10859–10869, Apr. 2012.

[37] K.-P. Ho and J. M. Kahn, "Statistics of group delays in multimode fiber with strong mode coupling," *J. Lightw. Technol.*, vol. 29, no. 21, pp. 3119–3128, Nov. 2011.

[38] R. Ryf *et al.*, "Space-division multiplexed transmission over 4200-km 3-core microstructured fiber," in *Proc. Opt. Fiber Commun. Conf.*, Los Angeles, CA, USA, 2012, Art. no. PDP5C.2.

[39] R. Ryf *et al.*, "1705-km transmission over coupled-core fibre supporting 6 spatial modes," in *Proc. Eur. Conf. Opt. Commun.*, Cannes, France, 2014, Art. no. PD.3.2.

[40] R. Ryf *et al.*, "Long-distance transmission over coupled-core multicore fiber," in *Proc. Eur. Conf. Opt. Commun.*, Düsseldorf, Germany, 2016, Art. no. Th.3.C.3.

[41] R. Ryf *et al.*, "Coupled-core transmission over 7-core fiber," in *Proc. Opt. Fiber Commun. Conf.*, San Diego, CA, USA, 2019, Art. no. Th4B.3.

[42] G. Rademacher *et al.*, "172 Tb/s C+L band transmission over 2040 km strongly coupled 3-core fiber," in *Proc. Opt. Fiber Commun. Conf.*, San Diego, CA, USA, 2019, Art. no. Th4C.5.

[43] D. Soma *et al.*, "50.47-Tbit/s standard cladding ultra-low-loss coupled 4-core fiber transmission over 9,150 km," in *Proc. Opt. Fiber Commun. Conf.*, 2021, Art. no. W7D.3.

[44] T. Fujisawa and K. Saitoh, "A group delay spread analysis of strongly coupled 3-core fibers: A effect of bending and twisting," *Opt. Express*, vol. 24, no. 9, pp. 9593–9591, May 2016.

[45] M. B. Shemirani, W. Mao, R. A. Panicker, and J. M. Kahn, "Principal modes in graded index multimode fiber in presence of spatial- and polarization-mode coupling," *J. Lightw. Technol.*, vol. 27, no. 10, pp. 1248–1261, May 2009.

[46] S. Fan and J. M. Kahn, "Principal modes in multimode waveguides," *Opt. Lett.*, vol. 30, no. 2, pp. 135–137, Jan. 2005.

[47] A. Mecozzi, C. Antonelli, and M. Shtaif, "Intensity impulse response of SDM links," *Opt. Express*, vol. 23, no. 5, pp. 5738–5743, Mar. 2015.

[48] C. Antonelli, A. Mecozzi, M. Shtaif, and P. J. Winzer, "Stokes-space analysis of modal dispersion in fibers with multiple mode transmission," *Opt. Express*, vol. 20, no. 11, pp. 11718–11733, May 2012.

[49] K. Saitoh, T. Fujisawa, and T. Sato, "Coiling size dependence of group delay spread in coupled multicore fibers without intentional twisting," *J. Lightw. Technol.*, vol. 35, no. 20, pp. 4559–4566, Oct. 2017.

[50] T. Sakamoto, T. Mori, M. Wada, T. Yamamoto, F. Yamamoto, and K. Nakajima, "Strongly-coupled multi-core fiber and its optical characteristics for MIMO transmission systems," *Opt. Fiber Technol.*, vol. 35, pp. 8–18, Feb. 2017.

[51] T. Sakamoto, T. Mori, M. Wada, T. Yamamoto, F. Yamamoto, and K. Nakajima, "Coupled few-mode multicore fiber with low differential mode delay characteristics," *J. Lightw. Technol.*, vol. 35, no. 6, pp. 1222–1227, Mar. 2017.

[52] T. Hayashi, Y. Tamura, T. Hasegawa, and T. Taru, "Record-low spatial mode dispersion and ultra-low loss coupled multi-core fiber for ultra-long-haul transmission," *J. Lightw. Technol.*, vol. 35, no. 3, pp. 450–457, Feb. 2017.

[53] K. Yoshida, T. Fujisawa, T. Sato, and K. Saitoh, "Optimum index profile of few-mode coupled multicore fibers for reducing the group delay spread," *Opt. Express*, vol. 27, no. 11, pp. 16281–16295, May 2019.

[54] Y. Yamada *et al.*, "Spatial mode dispersion control in a coupled MCF using high density cabling parameters," in *Proc. Opt. Fiber Commun. Conf.*, San Diego, CA, USA, 2020, Art. no. M4C.5.

Kunimasa Saitoh (Member, IEEE) received the B.S., M.S., and Ph.D. degrees in electronic engineering from Hokkaido University, Sapporo, Japan, in 1997, 1999, and 2001, respectively. From 2001 to 2005, he was a Research Associate with the Graduate School of Engineering, Hokkaido University. From 2005 to 2013, he was an Associate Professor with the Graduate School of Information Science and Technology, Hokkaido University, and in 2013 he became a Professor there. He is the author of more than 200 research papers in refereed international journals and 250 refereed conference presentations. His research interests include fiber optics, optical fiber communications, and optoelectronics. From 1999 to 2001, he was a Research Fellow of the Japan Society for the Promotion of Science. He is a Member of the Optical Society of America (OSA) and Institute of Electronics, Information and Communication Engineers (IEICE). He was the Chair of Subcommittee D4 of Optical Fiber Communication Conference (OFC) in 2016 and the Chair of Subcommittee SC1 of European Conference on Optical Communication (ECOC) in 2018. He was the recipient of the Excellent Paper Award and Young Scientist Award from the IEICE, in 1999 and 2002, respectively, Young Scientists' Prize of the Commendation for Science and Technology from the Ministry of Education, Culture, Sports, Science, and Technology (MEXT), Government of Japan in 2008, JSPS Prize from the Japan Society for the Promotion of Science in 2015, and Distinguished Lecturers Award from IEEE Photonics Society in 2017.